2014

CROSS PHOTOREACTION OF PYRUVIC AND GLYOXYLIC ACIDS IN MODEL AQUEOUS AEROSOLS

Shasha Xia
University of Kentucky, shasha.xia@uky.edu

STUDENT AGREEMENT:

I represent that my thesis or dissertation and abstract are my original work. Proper attribution has been given to all outside sources. I understand that I am solely responsible for obtaining any needed copyright permissions. I have obtained needed written permission statement(s) from the owner(s) of each third-party copyrighted matter to be included in my work, allowing electronic distribution (if such use is not permitted by the fair use doctrine) which will be submitted to UKnowledge as Additional File.

I hereby grant to The University of Kentucky and its agents the irrevocable, non-exclusive, and royalty-free license to archive and make accessible my work in whole or in part in all forms of media, now or hereafter known. I agree that the document mentioned above may be made available immediately for worldwide access unless an embargo applies.

I retain all other ownership rights to the copyright of my work. I also retain the right to use in future works (such as articles or books) all or part of my work. I understand that I am free to register the copyright to my work.

REVIEW, APPROVAL AND ACCEPTANCE

The document mentioned above has been reviewed and accepted by the student's advisor, on behalf of the advisory committee, and by the Director of Graduate Studies (DGS), on behalf of the program; we verify that this is the final, approved version of the student's thesis including all changes required by the advisory committee. The undersigned agree to abide by the statements above.

Shasha Xia, Student

Dr. Marcelo I. Guzman, Major Professor

Dr. Dong-Sheng Yang, Director of Graduate Studies

CROSS PHOTOREACTION OF PYRUVIC AND GLYOXYLIC ACIDS IN MODEL AQUEOUS AEROSOLS

THESIS

A thesis submitted in partial fulfillment of the
requirements for the degree of Master of Science in the
College of Arts and Science
at the University of Kentucky

By

Shasha Xia

Lexington, Kentucky

Director: Dr. Marcelo I. Guzman, Professor of Chemistry

Lexington, Kentucky

2014

ABSTRACT OF THESIS

CROSS PHOTOREACTION OF PYRUVIC AND GLYOXYLIC ACIDS IN MODEL AQUEOUS AEROSOLS

Aerosols affect climate change, the energy balance of the atmosphere, and public health due to their variable chemical composition, size, and shape. Aerosols from natural and anthropogenic sources can be primary organic aerosols (POA), which are directly emitted to the atmosphere, or secondary organic aerosols (SOA) that are formed from chemical reactions of gas-phase precursors. At variance with the well investigated formation of SOA from gas phase precursors, the chemistry of aqueous SOAs that contribute to the total SOA budget remains unknown. Field measurements have revealed that carboxylic, dicarboxylic and oxocarboxylic acids are abundant species present in SOAs. This thesis explores the fate of two such acids, pyruvic (PA) and glyoxylic (GA) acids surrogates of the oxocarboxylic acids in the atmosphere, in their cross reaction under solar irradiation and dark thermal aging. Mixtures of complex photoproducts are identified by ion chromatography (IC) with conductivity and electrospray (ESI) mass spectrometry (MS) detection, direct ESI-MS analysis in the negative ion mode, and nuclear magnetic resonance spectroscopy (NMR) analysis including one-dimensional (^{1}H- and ^{13}C-NMR) and two-dimensional techniques such as gradient correlation spectroscopy (gCOSY) and heteronuclear single quantum correlation (HSQC). A reaction mechanism for the cross reaction is provided based on all experimental observations.

KEYWORDS: Aqueous Secondary Organic Aerosols, Photochemistry of Organic Acids, Oxocarboxylic Acids, Electrospray Ionization Mass Spectrometry, Multiple Nuclear Magnetic Resonance Spectroscopy Analysis

Shasha Xia

July 30, 2014

CROSS PHOTOREACTION OF PYRUVIC AND GLYOXYLIC ACIDS IN MODEL AQUEOUS AEROSOLS

By

Shasha Xia

Marcelo I. Guzman, Ph.D.
Director of Thesis

Dong-Sheng Yang, Ph.D.
Director of Graduate Studies

July 30, 2014
Date

Acknowledgements

I would like to express my deeply appreciation to my advisor Dr. Marcelo Guzman for all his guidance, support, and encouragement for both my course study and research work during these three years, especially in the period for preparation of this thesis. He also provided me a lot of helpful and precious advice for my future life that I will benefit from for the rest of my life. I would like to thank my committee members, Dr. Dong-Sheng Yang and Dr. Folami Ladipo, for their time invested in my education and for providing valuable feedback about my research. The great help that Mr. John Layton provided me during NMR training has been instrumental to obtain the related results reported in this thesis. In addition, I would like to express my gratitude to all my labmates, especially to Alexis Eugene, Ruixin Zhou, and Elizabeth Pillar. Thank you for all the generous help on my research and also to the great times we have spent together in the past three years. Finally, I would like to say thank you to my family and friends, for their constant support and encouragement through the years.

TABLE OF CONTENTS

List of Tables

List of Figures

List of Schemes

Section 1: Introduction

Aerosols play a vital role in the chemistry and physics of the atmosphere affecting climate change and public health.[1-3] Aerosols can contribute to air pollution having detrimental effects on human health associated to cardiovascular and respiratory problems.[2,4,5] Atmospheric aerosols can affect the Earth's energy balance because they directly scatter and absorb solar radiation, and indirectly participate in the condensation of clouds and ice nuclei.[1,6,7] Aerosols contribute to the surface cooling effect by scattering solar radiation and increasing the reflectance of clouds and precipitation.[8] Contrarily, aerosols that absorb radiation are an additional contribution to global warming.[9,10] Aerosols also behave as reactors for important multiphase processes and heterogeneous reactions.[11-14] Organic aerosols (OAs) possess the largest uncertainty in the radiative budget of the atmosphere,[10] an issue that demands ongoing research efforts.[15] Addressing this uncertainty requires studying the related optical properties of OAs, which are determined by their variable and complex particle size, structure, and chemical composition.[10,16] Understanding the sources, transformation, and reactive processing of OAs is an active focus of research that started during the past decades.[10] However, the lack of a complete model to explain these issues requires further research efforts to obtain a comprehensive representation of OAs in climate models.

Aerosols in the atmosphere, whether from natural or anthropogenic sources, include primary organic aerosol (POA) and secondary organic aerosol (SOA).[9] POA is directly emitted to the atmosphere as mineral dust, sea salt, and primary biological aerosol particles (PBAPs) from natural origins or as black carbon (BC), nitrate, and ammonium from anthropogenic sources. SOA is formed through chemical reactions of gas-phase

precursors, such as biogenic volatile organic compounds (VOCs), NO_x, and SO_2, which comes from both natural and anthropogenic (e.g., cooking, vehicles, etc.) sources.[9,10] There is a general understanding that the processing of VOCs can proceed through 1) gas-phase reactions by hydroxyl radical ($HO^{\bullet}$), NO_3, or O_3, 2) aqueous-phase reactions of carbonyl compounds and carboxylic acids, and 3) heterogeneous reactions.[13] Recent field studies that have tried to quantify the yield of SOA from known emission sources concluded that the majority of models underestimate SOA production.[17-19] Although alternative models based on field measurements of BC and OA concentrations in the Arctic considered deposition processes,[20] and valuable information was extracted from examining the vertical[21] and regional[22] distribution of OA, the existence of missing sources of SOA production is recognized and needs to be addressed.[21] While SOA formation from gas-phase precursors is relatively well understood, it cannot close the gap between measurements and known production mechanisms of SOAs. For the previous reason, it has been suggested that aqueous-phase chemistry could contribute to explain the total SOA budget.[12,23] Thus, this research is focused on the identification of the missing mechanisms of SOA production by investigating reactions in the aqueous-phase. This thesis 1) explores how atmospheric chemical reactions of interest proceed in atmospheric water mimics affecting the optical properties of model aqueous SOAs (aqSOAs), 2) identifies the reaction products, 3) and measures the time series of products involved in the reaction mechanism.

Among all the species found in aqSOAs, 2-oxocarboxylic acids, such as pyruvic (PA) and glyoxylic acids (GA) are widely present in different environments. Atmospheric photooxidation of isoprene[24-26] and aromatics[27,28] produce first generation products such

as methylglyoxal, glyoxal, phenol and benzaldehyde. In more detail, GA can be directly produced from $HO^{\bullet}$ attack on glyoxal, glycolic acid or hydroperoxy acetic acid,[29] while PA results from atmospheric processing of methylglyoxal.[30] Field measurements showed that GA is the most abundant 2-oxocarboxylic acid present in OAs, followed by PA.[31-33] Assuming that the upper limit to the water content of aerosol droplets is determined by the deliquescence curve of an ammonium bisulfate solution[34,35] at 50 % relative humidity (RH), the droplets in aerosols contain 0.6 g of H_2O/g of SO_4^{2-} or [PA] > 20 mM under very acidic conditions.[36] Similarly, the concentration of GA in arctic SOA can be estimated,[37] to be as high as 287 mM, for a molar ratio [GA]/[PA] ~ 8-14. Even higher concentration could be used in laboratory experiments that simulate a polluted environment, because the level of PA and GA in a city such as Tokyo can exceed by 30 and 3 times, respectively, those measured in the pristine Arctic aerosol.[37,38]

The chemical fate of PA by direct[36,39] and indirect[24] photoreactions is the subject of continuous research. However, the direct photoreaction of GA, the cross photoinduced reaction of species typically present together such as PA and GA, and the possible associated mechanisms for these processes that have remained unexplored are approached for the first time in this work. The experimental work herein reports how sunlight can trigger the cross reaction of GA and PA, which is followed by thermal reactions during dark periods. The identification of complex photoproducts is carried out by 1) ion chromatography with dual conductivity and electrospray (ESI) mass spectrometric detection (IC-MS), 2) direct ESI-MS analysis in the negative ion mode, 3) nuclear magnetic resonance spectroscopy (NMR) analysis including one-dimensional (^{1}H- and ^{13}C-NMR), and two-dimensional gradient correlation spectroscopy (gCOSY)

and heteronuclear single quantum correlation (HSQC) experiments. Experimental conditions of ionic strengths, temperature, and photon flux are chosen to simulate those encountered by nascent sea spray aerosols. The model starting mixtures contain *ca.* [PA] = 28 mM and [GA] = 236 mM, which are exposed to UV-visible light in the range of surface solar radiation. The variables under study include samples with and without the most abundant electrolytes in seawater ($[Na^+]$ = 468 mM, $[Cl^-]$ = 545 mM and $[SO_4^{2-}]$ = 28.2 mM)[40] under a 1 atm N_2(g), 1 atm O_2(g), and 1 atm air. This work presents an advanced analysis that contrasts how the chemical composition and optical properties of model aqSOAs vary during photochemical and thermal processes. Based on the information gathered, a mechanism for the cross reaction of PA and GA that agrees with all experimental observations is finally presented.

Section 2: Materials and Experimental Methods

2.1. Preparation of experiments and controls

A mixture of 50 mM PA (Sigma-Aldrich, 99.1 %) and 300 mM GA (Sigma-Aldrich, 50 wt. % in H_2O) was prepared daily in ultrapure water (Elga Purelab flex, 18.2 MΩ cm^{-1}). The mixture of acids was doped with inorganic electrolytes including $[Na^+]$ = 468 mM, $[Cl^-]$ = 545 mM and $[SO_4^{2-}]$ = 28.2 mM prepared from NaCl (Fisher, 99 %), Na_2SO_4 (Fisher, 99 %) and HCl (EMD, 38 %). The mixture was adjusted to pH =1.0 with [HCl] = 2.0 M, and 180 mL were transferred to customized fused silica photoreactor of 220 mL capacity. The reaction vessel was sealed and the reaction temperature was controlled at 298 K by circulating ethanol (Ricca, 69.6% v/v) through the jacket with a bath circulator

(Thermo Scientific, A25). Solutions underwent continuous and gentle sparging through a septum at a flow rate of 100 mL min^{-1} with 1 atm air (Scott-Gross, UHP) starting 30 minutes before photolysis. The control experiments in Table 1 were designed to study the effect of inorganic electrolytes and the concentration of O_2 (g) on the cross reaction of PA and GA, and included: Control A under 1 atm N_2(g) (Scott-Gross, UHP), control B under 1 atm O_2(g) (Scott-Gross, UHP), control C without electrolytes, control D without electrolytes under 1 atm N_2(g), and control E without electrolytes under 1 atm O_2(g).

Table 1. Experiments and controls to investigate the cross reaction of PA and GA

	Conditions				
	$h\nu$	Electrolytes	Atmosphere		
			Air	N_2	O_2
Experiment	✓	✓	✓		
Control A	✓	✓		✓	
Control B	✓	✓			✓
Control C	✓		✓		
Control D	✓			✓	
Control E	✓				✓
Control F		✓	✓		

Table key: $h\nu$ indicates the presence of light. Electrolytes include Na^+, Cl^- and SO_4^{2-}.

2.2. Photochemical experiments and thermal treatment of photolyzed samples

The photochemical setup employed is depicted in Scheme 1 and includes a 1 kW high-pressure Xe-Hg lamp (Newport). A water filter was used (Newport) to remove unwanted infrared radiation, and a cut-on filter (Oriel) at $\lambda \geq 305$ nm provided actinic radiation in the solar window. Potassium ferrioxalate (Alfa Aesar, 98.9 %) was used as an actinometer to measure the actinic flux (1.06×10^{-5} Einstein s^{-1} for $\lambda \geq 305$).[41] During the first stage of processing (Stage I in Scheme 2), samples of the experiment and controls (Table 1) were irradiated for 6 h and 5 mL aliquots were withdrawn from the reactor at 0, 0.5, 1, 2, 3, 4, 5, and 6 h. A 30 % of the aliquot was immediately frozen at – 20 °C and stored in the dark for later analyses by IC-ESI-MS, direct ESI-MS, and NMR spectroscopy. The remaining 3.5 mL of sample was transferred to a Suprasil cuvette (Starna Cells, 10-mm optical path length) to monitor its aging (Stage II in Scheme 2) in the dark by UV-visible spectroscopy for 15 h at 298 K followed by 9 h at 323 K. The same analyses performed to the irradiated samples was also applied to the aged samples after dark periods.

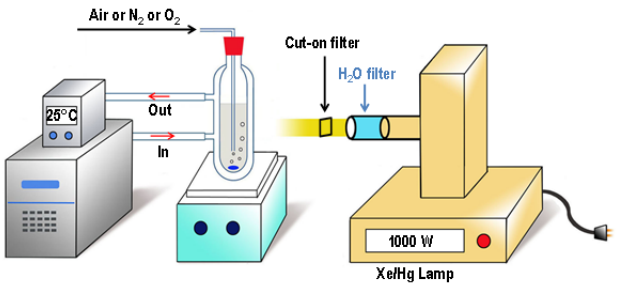

Scheme 1. Experimental setup.

About 130 mL of the remaining photolyzed sample was stored in the dark for 24 h and then re-photolyzed (Stage III in Scheme 2) under the same conditions previously described. The later re-photolyzed samples underwent a second aging process in the dark monitored by UV-visible spectroscopy (Stage IV in Scheme 2). Similarly, the same set of experiments and controls listed in Table 1 is used to study the photochemical conversion of individual samples of 26.0 mM PA and 252.1 mM GA, photolyzed during 2 and 8 h, respectively. This supporting information is available in section 5 of the thesis.

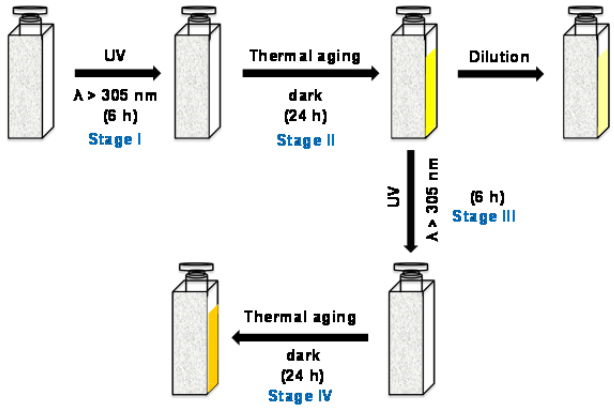

Scheme 2. Representation of the processing of pyruvic (PA) and glyoxylic (GA) acids mixture. Stages I and III are both 6 h photolysis periods. Stages II and IV each refer to (dark) thermal aging during 15 h at 298 K followed by 9 h processing at 323 K.

2.3 Analysis of products

Samples were analyzed by 1) UV-visible spectroscopy, 2) ion chromatography (IC) equipped with a conductivity detector and a mass spectrometer (MS) interfaced with an

electrospray ionization (ESI) probe (IC-ESI-MS), 3) direct infusion electrospray mass spectroscopy (ESI-MS), and 4) a combination of nuclear magnetic resonance spectroscopy (NMR) experiments including one dimensional (1D) ^{1}H- and ^{13}C-NMR, and two dimensional (2D) gradient correlation spectroscopy (gCOSY) and heteronuclear single quantum correlation (HSQC). The uncertainty associated with UV-visible spectroscopy, IC-MS, and ESI-MS measurements, based on the propagation of systematic errors,[42] is lower than 1.0 %.

UV-visible spectra ($190 \leq \lambda \leq 750$ nm) of initial and irradiated samples were recorded immediately after sampling with an Evolution 220 scanning spectrophotometer (Thermo Scientific) equipped with a temperature control multi-cell holder (Thermo Scientific, SPE 8 W). In addition, spectra were recorded during the aging processing every 30 min. Actual initial concentrations of PA and GA in the mixture were deconvoluted from total absorbance using Beer's Law and the calculated molar absorptivity of pure PA (ε_{PA} = 11.3 M^{-1} cm^{-1} at λ = 320 nm)[27] and GA (ε_{GA} = 11.6 M^{-1} cm^{-1} at λ = 240 nm)[43] standard solutions in water. Multiple wavelengths (λ = 260, 270, 280, 290, 300, and 320 nm) were chosen to calculate the molar absorption coefficient for each component in its standard and the contribution of each species to the total absorbance in the mixture. The molar absorptivities were calculated for PA (ε_{260} = 26.7 M^{-1} cm^{-1}, ε_{270} = 7.5 M^{-1} cm^{-1}, ε_{280} = 5.0 M^{-1} cm^{-1}, ε_{290} = 5.7 M^{-1} cm^{-1}, ε_{300} = 7.6 M^{-1} cm^{-1}, and ε_{320} = 11.3 M^{-1} cm^{-1}) and GA (ε_{260} = 2.6 M^{-1} cm^{-1}, ε_{270} = 2.5 M^{-1} cm^{-1}, ε_{280} = 2.2 M^{-1} cm^{-1}, ε_{290} = 1.7 M^{-1} cm^{-1}, ε_{300} = 1.4 M^{-1} cm^{-1}, and ε_{320} = 1.0 M^{-1} cm^{-1}) using Beer's Law equation

$$A = \varepsilon\, b\, [X] \qquad (1)$$

for a path length b = 1.0, and the measured absorbance of individual standard solutions of [PA] = 28.8 mM and [GA] = 90.3 mM. Microsoft Excel Solver was used to solve the actual concentrations for PA and GA in the mixture, which were [PA] = 27.9 mM and [GA] = 235.6 mM.[42] More details about this calculation can be found in the supporting information in section 5.

Samples for ion chromatography were diluted 500 times with ultrapure water before injection with an autosampler (Dionex AS) in an IC (Dionex ICS-2000) provided with an IonPack AS11-HC (2 mm) analytical column and a conductivity detector. An ESI probe interfaced the output of the conductivity detector to a mass spectrometer (Thermo Scientific, MSQ Plus). The same chromatographic and mass spectrometer conditions previously established by Zhou and Guzman (2014) are used in this work.[44] Briefly, the initial 1 mM potassium hydroxide concentration at a flow of 0.38 mL min^{-1} increases following three linear gradient steps (1.4 mM min^{-1} up to 15 mM, 1.5 mM min^{-1} up to 30 mM, and 3.0 mM min^{-1} up to 60 mM).[44] For direct infusion analysis, samples are diluted 1000 times with ultrapure water and injected in the ESI-MS, which is operated in negative ion mode at 70 psi nitrogen nebulizing gas, 450 °C, 2.4 kV needle voltage, and 40 V cone voltage, unless otherwise indicated in the text.

The NMR (Varian INOVA 400) spectra at room temperature is recorded using a 5-mm NMR tube (Wilmad) with 540 μL of sample spiked with 60 μL D_2O (Cambridge Isotope, 99.9 %), for field-frequency lock doped with 3-(trimethylsilyl)-1-propanesulfonic acid sodium salt (DSS, Sigma-Aldrich, 97 %) internal standard. A water suppression enhanced through T_1 effects solvent suppression (WET) method is applied

using VnmrJ 3.2 software to eliminate more than 99.3% of the H_2O signal. Further details of the NMR methods can be found in the supporting information in section 5.

Section 3: Results and Discussion

3.1. Optical properties

UV-visible spectroscopy is used to study the optical property of the mixture of PA and GA under the variable conditions listed in Table 1. Figure 1 displays the UV-visible absorption spectra of a mixture with 27.9 mM pyruvic acid (PA) and 235.6 mM glyoxylic acid (GA) before and after photolysis in the presence of electrolytes under 1 atm air (experiment in Table 1) for the four stages listed in the experimental section (Scheme 2). The spectrum corresponding to the sample before irradiation shows a peak at $\lambda = 321$ nm from PA, and a shoulder at $\lambda = 276$ nm due to GA. After 6 h of irradiation, the absorption spectrum displays the loss of carbonyl functionalities in the ultraviolet portion resulting from photobleaching occurring during stage I. For the following 24 h of thermal aging in stage II, an absorbance increment or thermochromism is observed. For the second irradiation period, which simulates a second daytime cycle (stages III), photobleaching produces a practically identical spectrum than the one observed at the end of stage I. Similarly, thermochromism in dark stage IV, a second nighttime cycle, recovers the high absorption developed during stage II.

The observed evolution of “brown” carbon species in the mixture of products is related to the presence of alcohol, aldehyde, and ether groups that are characterized

below by several spectroscopic techniques. Under mild atmospheric conditions in the dark, these functional groups react with low activation energy barriers to produce chromophoric species. For example, the self-condensation of aldehydes,[45,46] the formation of alkenes from alcohols,[47] and the esterification of acids,[48] are viable atmospheric reactions. Particularly, unsaturated hydrocarbons can undergo facilitated hydration in the presence of light,[49] which explains the photobleaching registered in the UV-visible spectra.

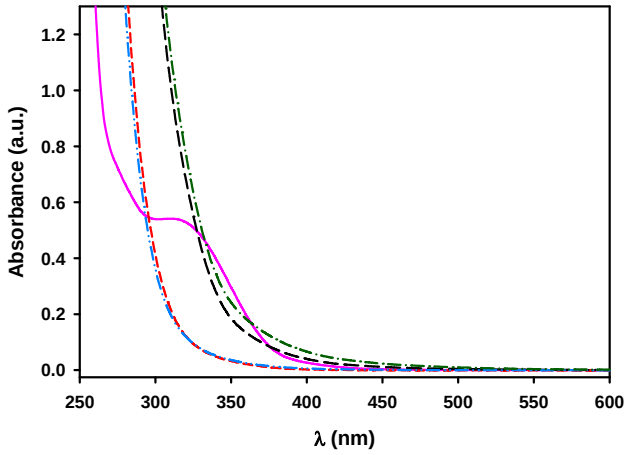

Figure 1. UV-visible absorption spectra (pink solid line) before photolysis, (red short dashed line) post-photolysis at the end of stage I; (black dashed line) followed by 15 h of thermal aging at 298 K and 9 h at 323 K in stage II, (blue dash-dot-dot line) after a second 6 h photolysis in stage III, and (green dash-dot line) after a second thermal aging in stage IV. Experimental conditions: Mixture of [PA] = 27.9 mM, [GA] = 235.6 mM, $[Na^+]$ = 545 mM, $[SO_4^{2-}]$ = 28.2 mM, and $[Cl^-]$ = 468 mM, at pH = 1.0 under 1 atm air.

Figure 2 shows the normalized areas integrated under the UV-visible absorption spectra during the four processing stages (Scheme 2) for an experiment and controls in Table 1 for the wavelength interval bracketed by λ_{min} = 295 nm to λ_{max} = 500 nm. For normalization, all integrated areas were divided by its initial area before irradiation. Control F in the absence of light remained stable over the four stages and is not included in Figure 2. There is a large contrast between stages I and III under irradiation displaying photobleaching and dark stages II and IV corresponding to thermochromism during aging.[50] Each half cycle, daytime *versus* nighttime simulation conditions, shows a complete different dependance on the presence of inorganic electrolytes and [O_2(aq)].

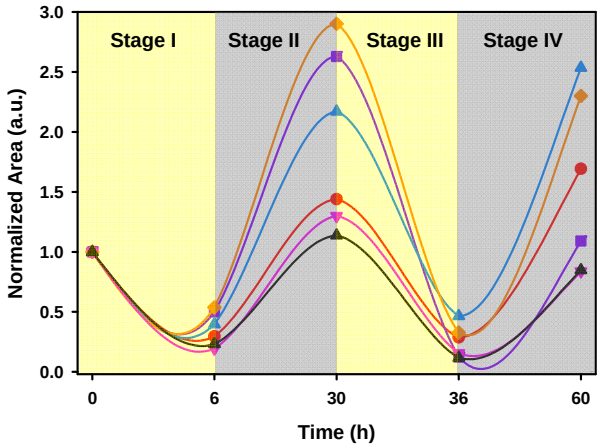

Figure 2. Normalized area (λ_{min} = 295 nm and λ_{max} = 500 nm) under the UV-visible absorption spectra for (red ●) an experiment, (blue ▲) control A in N_2,(pink ▼) control B in O_2, (violet ■) control C without electrolytes, (orange ♦) control D without electrolytes in N_2, and (black ▲) control E without electrolytes in O_2. Experimental conditions defined in Figure 1 and controls given in Table 1.

Applying Henry's law to calculate [O_2(aq)] at 298 K from its equilibrium partial pressure in air (P_{O_2}= 0.2095 atm) or in a pure O_2(g) atmosphere:

$$[O_2(aq)] = K_H\, P_{O_2} \tag{2}$$

with Henry's law constant K_H = 1.28 × 10^{-3} M atm^{-1}, then [O_2(aq)] = 0, 0.26, and 1.24 mM for 1 atm N_2(g), air, and O_2(g), respectively. In the previous calculation, the contribution of the partial pressure of water at 298 K (P_{H_2O} = 0.0313 atm) is subtracted.[51]

Although some minor changes are observed at the end of the first photobleaching in stage I of Figure 2, thermochromism becomes pronounced during stage II. Once stage II is complete, a comparison of the effect of [O_2(aq)] (experiment, control A, and control B in Table 1) in the presence of electrolytes, reveals that for higher O_2 levels thermochromism becomes less prominent relative to the initial values. The ratio of areas after stage II to the initial value before photolysis increases in the order O_2(g) < air < N_2(g): 1.30 < 1.44 < 2.17. The same qualitative conclusion is valid for the subset of experiments in the absence of electrolytes (controls C, D, and E). The direct effect of electrolytes in thermochromism of stage II can be compared for the pair of subsets in air (experiment and control C), in N_2(g) (controls A and D), and in O_2(g) (controls B and E). The results show that the lack of electrolytes in the sample benefits the development of thermochromism in air, which increases in N_2(g) but drops in pure O_2(g). In stage III a second photobleaching cycle starts, and a change in the areas is perceived when comparing samples with and without electrolytes in N_2(g) and air. During stage IV, a reversal in the magnitude of the areas is observed for the pairs experiments and control C, controls A and D, and controls B and E. However, the previous absorption enhancement

due to the presence of electrolytes is much less pronounced for the latter case in 1 atm O_2(g).

In summary, the presence of O_2 is detrimental for the formation of chromophores. Electrolytes play a significant different role enhancing thermochromism in stage IV and diminishing it in stage II. The previous observation implies that the formation of complex polyfunctional $C_xH_yO_z$ oligomers during stages I and II contribute to the production of less oxygenated species (shown in Figure S1). These species react undergoing thermochromism through interaction with electrolytes after stage III. It is important to contrast present results with previous experiments for the self-reaction of PA.[50] While a previous study was focused on the optical properties of complex organic matter from higher 80 mM PA in 2 M ammonium bisulfate (ABS), this work investigates the behavior of more diluted ~ 28 mM PA with a mixture of electrolytes ($[Na^+]$ = 545 mM, $[Cl^-]$ = 468 mM, and $[SO_4^{2-}]$ = 28.2 mM) that does not include NH_4^+. The analysis of photobleaching and thermochromism during two cycles, each for controls G to M (Table S1, Supporting Information) with 26.0 mM PA (no GA) is available in Figure S2 (Supporting Information). The effect of electrolytes in Figure S2 agrees well with previous observations[50] that electrolytes enhance the observed thermochromism of PA alone during stages II and IV. Thermochromism increases with higher ionic strength (from inert electrolytes) and temperature, which promotes the dehydration of hydroxyl functional groups in alcohols >CH-C(OH)< to form olefin groups >C=C<.[50] Then, the inverse process of hydration of unsaturated carbon is facilitated through photoinduced reactions in water.[50] However, for the mixture of PA and GA, electrolytes play a major role in the development of thermochromism, an important observation for aged organic matter

produced in situ in atmospheric waters. The presence of GA in our samples represents a typical species that can alter the reactivity of PA by cross-reactions, affecting the composition of aged complex organic matter, which possess a higher O/C ratio of 0.83-1.2 comparing with 0.71-1 in PA (no GA) photoproducts.

Figure 3A presents the absorption changes and linear regression at selected wavelengths (λ = 280, 295, 320, 350, 420, 450 and 500 nm) for the same experiment in Figure 1 (after stage II) upon successive dilutions with H_2O by a factor f^{-1} = 1, 0.5, 0.25, and 0.1. Beer's Law is followed well only for the UV and shorter visible range ($\lambda \leq 350$ nm). Figure 3B shows large changes in the coefficient of determination (R^2) of the linear regressions at the fixed λ. Figure 3B allows to compare the experiment and controls with 1 atm O_2(g) or N_2(g), or without electrolytes by exploring the linearity at variable λ every 5 nm. The effect of [O_2(aq)] in the dispersion of R^2 values can be compared between the experiment (red circles), and controls A (blue triangles) and B (pink triangles). It is interesting to compare the R^2 values for a transition from pure air to N_2, which represents the decrease of O_2 levels as altitude rises in the actual Earth's atmosphere. It is apparent that Beer's Law is less obeyed starting above λ = 470 nm in pure N_2 than in air. The larger drop of the trend in control C (violet squares) than for the experiment indicates that the presence of inorganic electrolytes is less important than the presence of O_2 to affect the R^2 values.

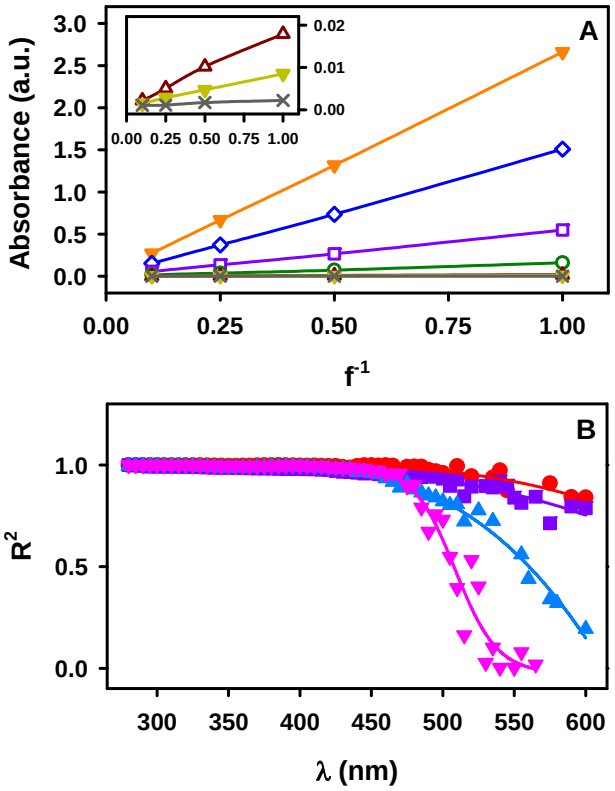

Figure 3. (A) Absorbance of mixtures in the experiment of Figure 1 at the end of stage II (Scheme 2 and Figure 2) *vs.* dilution factor (f^{-1}) at λ: (orange ▼) 280, (dark blue ◊) 295 nm, (violet □) 320, (dark green ○) 350, (brown ∆) 420, (dark yellow ▽) 450, and (grey ×) 500 nm. (B) Coefficient of determination (R^2) for linear regression fittings in part A for (red ●) an experiment in Figure 1, (blue ▲) control A in1 atm N_2(g), (pink ▼) control B in1 atm O_2(g), and (violet ■) control C in 1 atm air without electrolytes.

It is clear from these findings that the complex chemical composition of the reaction products affects the optical properties of mixtures that represent the organic matter found in atmospheric waters. The multiple functional groups present in the photolyzed and thermally aged samples behave as absorbing species but can also scatter light in the

presence of electrolytes.[39,50] The presence of electrolytes and dissolved O_2 do affect the chemical reactivity of the organic species upon irradiation and thermal aging. Therefore, the daytime and nighttime cycles that the experiment simulates reflect how organic species in the atmosphere behave and should be treated in future climate change models taking into account thermochromism and photobleaching parametrization factors. This issue should be the focus of future combined modeling and experimental efforts, accounting for the facts that the composition of organic aerosols varies with geographical location, altitude, and time of the day.[39,50]

3.2. Identification of products

Among the several methods used to study the cross reaction products of PA and GA mixtures, useful information is provided by analyzing 1) IC-ESI-MS chromatograms of photolysis products, and 2) direct infusion ESI-MS. The information from direct infusion ESI-MS reveals the the mass-to-charge ratio (*m/z*) for all anionic products present in the sample. IC-ESI-MS also provides *m/z* values, but after chromatographic separation of the mixture, which eliminates possible artifacts caused by infusing a mixture of products directly. The data below shows that both methods report a similar product composition in the experiment and control C, suggesting that the presence of inorganic electrolytes does not determine the formation of products.

Figure 4 shows a pair of IC chromatograms with conductivity and ESI-MS detection in the negative ion mode for the same experiment in Figure 1 before (A) and after (B) 6 h photolysis. Before irradiation, peaks 1 through 4 eluting at 6.624, 10.674, 11.900 and

19.487 min in the conductivity detector are assigned with matching standards and by their *m/z* values to pyruvate ($C_3H_3O_3^-$, *m/z* 87), glyoxylate ($C_2H_1O_3^-$, *m/z* 73), chloride (Cl^-), and bisulfate (HSO_4^-, *m/z* 97), respectively.

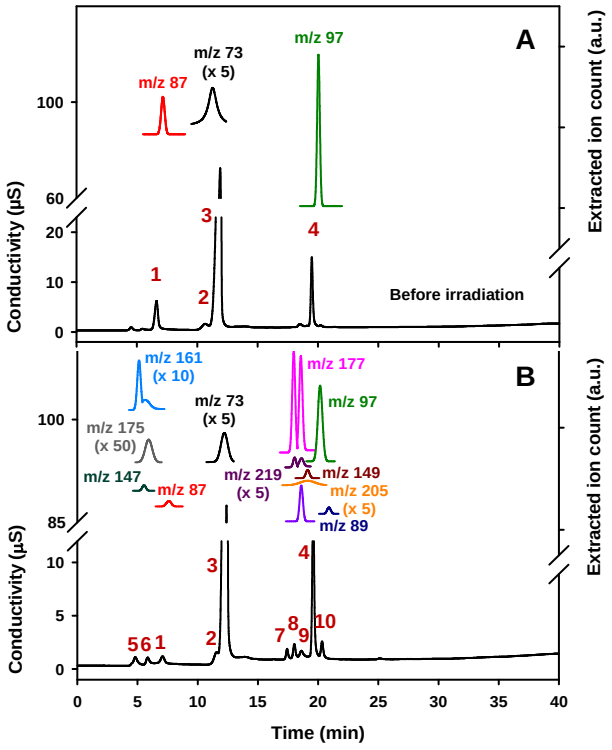

Figure 4. Ion chromatogram with conductivity and ESI-MS (-) detection for the experiment in Figure 1 (A) before and (B) after 6 h of irradiation. Key for peaks: (**1**) PA (*m/z* 87), (**2**) GA (*m/z* 73), (**3**) chloride, (**4**) sulfate (*m/z* 97) (**5**) $C_6H_9O_5^-$ (*m/z* 161), (**6**) $C_5H_7O_5^-$ (*m/z* 147), a shoulder of $C_6H_9O_5^-$ (*m/z* 161), and 2-(3-oxobutan-2-yloxy)-2-hydroxypropionic acid ($C_7H_{11}O_5^-$, *m/z* 175), (**7**) a diastereomer of 2,3-dimethyltartaric acid ($C_6H_9O_6^-$, m/z 177), (**8**) a second diastereomer of 2,3-dimethyltartaric acid and $C_5H_7O_6^-$ (*m/z* 163), (**9**) tartaric acid (*m/z* 149), and (**10**) oxalic acid (*m/z* 89).

Upon 6 h of photolysis, new peak 6, 7, and 8 elute in Figure 4B, and correspond to the products from the self-photoreaction of PA (Figure S3),[36,52] 2-(3-oxobutan-2-yloxy)-2-hydroxypropionate ($C_7H_{11}O_5^-$, *m/z* 175) and two diasteromers of 2,3-dimethyltartrate ($C_6H_9O_6^-$, *m/z* 177). Peaks 9 and 10 are assigned to a trace of tartrate ($C_7H_{11}O_5^-$, *m/z* 149, a self-reaction product of GA) eluting at 19.086 min, and to a trace of oxalate ($C_2H_1O_4^-$, *m/z* 89, at 20.937 min), as observed in the photolysis of GA alone (Supporting Information Figure S4). Three additional new peaks labeled 5, 6, and 8 appear in the conductivity detector due exclusively to the cross-reaction of PA with GA. However, some conductivity peaks correspond to overlapping species based on the distinctive *m/z* values extracted with the help of the MS detector. For example, peak 6 contains anions at *m/z* 147, 161, and 175, while peak 8 includes the anions at *m/z* 177 and 163, which can be resolved as extracted ions. However, because the species at *m/z* 163 is absent in experiments with pure PA or GA, this species must be a cross photolysis product of PA and GA (Supporting Information Figures, S3 and S4). The extracted ion count at *m/z* 175 and 177 shows that there are one and two peaks in the chromatogram (Figure 4B) for each of them, respectively. The peak eluting at 5.796 for *m/z* 175 is assigned to 2-(3-oxobutan-2-yloxy)-2-hydroxypropionate,[36] whose area growths at longer irradiation times. The other major photoproducts with a formula mass of 178 Da originate from the self-reaction of PA, and elute closely at 17.927 and 18.538 min in the conductivity detector (peaks 7 and 8 in Figure 4B). The peaks can tentatively be assigned to 1) the two diastereomers (2R,3R and 2R,3S) of 2,3-dimethyltartaric acid (shown in Figure S5) or 2) the production of two different molecules from the combination of ketyl radicals of PA, $K^{\bullet}$, as shown in Scheme 3. In conclusion, peaks 5, 6 and 8 contain completely new

species with molecular mass of 162 Da, 148 Da and 164 Da resulting from the cross reaction of PA and GA. Based on the overlapping retention times of the new peaks with a mass difference of 14 Da (a -CH_2 group), 2-(3-oxobutan-2-yloxy)-2-hydroxypropionic acid and 2,3-dimethyltartaric acid, the new species in peak 6 and 8 are believed to have similar structures to the coeluting species with *m/z* 161 and 163, respectively.

Figure 5 shows the ion count change for PA, GA, and photoproducts during the initial photolysis stage obtained by ESI-MS (Figure 5A) and IC-ESI-MS (Figure 5B). GA *(m/z* 73), PA (*m/z* 87), and a cluster of PA (*m/z* 175) decay in the time series of Figure 5A. The decrease of the species at *m/z* 175 in Figure 5A corresponds to the parent peak of PA, and results from a monovalent anionic cluster of 2 × PA (87 + 88 = 175). The kinetics of exponential PA and GA loss during photolysis (in stage I) in Figure 5 corresponds to a first order reaction on the concentration of both reactants.[53] Three species that grow with irradiation time have a formula mass of 162, 164, and 178 Da. Figure 5B shows how the areas under chromatographically separated extracted ion peaks change for reactants and photoproducts. The latter method allows the identification of species that could co-elute at the same retention time by distinguishing their different *m/z* values. The species eluting at 4.8 min (*m/z* 161), 5.9 min (*m/z* 175 and 161), 18.0 min (*m/z* 177), 18.6 min (*m/z* 177, 163) grow exponentially over time in Figure 5B. However, the area for the peak at *m/z* 175 reaches a steady level during the beginning stage of photolysis. A comparison to the results from PA photolyzed controls G to M (Table S1, Supporting Information) indicates that the efficiency for the production of 2-(3-oxobutan-2-yloxy)-2-hydroxypropionic acid (*m/z* 175) is largely diminished by the presence of GA.

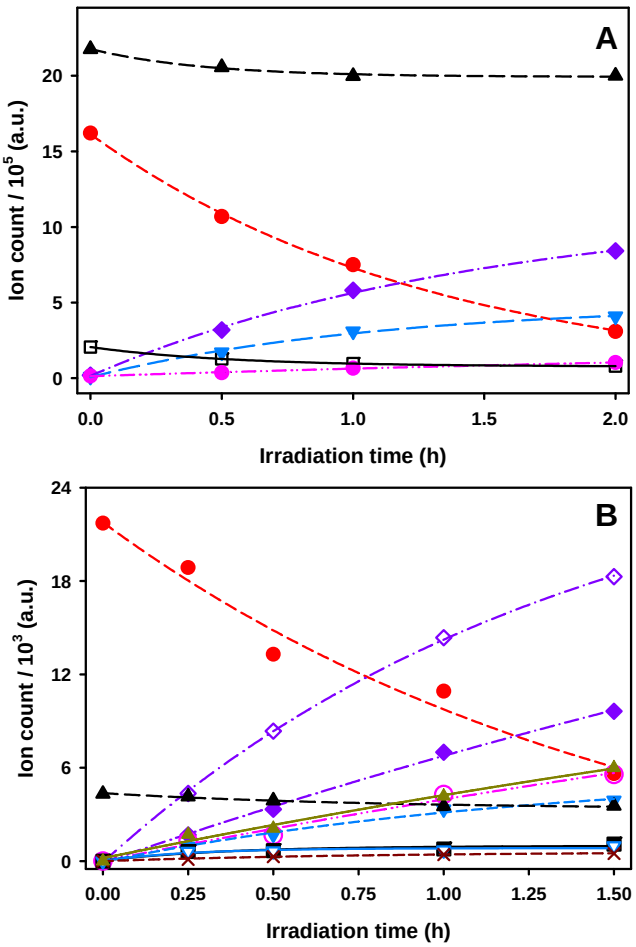

Figure 5. (A) Ion count from direct infusion ESI-MS(-) and (B) areas under the extracted IC-MS chromatographic peaks of species during the beginning of photolysis (stage I) for the experiment in Figure 1. Anions correspond to *m/z* (black ▲) 73, (red ●) 87, (brown ×) 89, (dark yellow ▲) 147, (blue empty ▽ and filled ▼) 161, (pink empty ○ and filled ●) 163, (black empty □ and filled ■) 175, and (violet ♦ and ◊) 177.

Figure 6 shows the results from direct infusion ESI-MS measurements reflecting the composition of an experiment with PA and GA during 6 h photolysis. The composition matches the *m/z* values observed during the beginning of photolysis by ESI-MS and IC-

MS in Figure 5. Figure 6 confirms that no product heavier than 250 Da is observed during irradiation in samples diluted 1000-times. The compounds in Figure 6 with formula mass of 128 and 130 Da can be described as clusters of the most abundant (99.67 %) gem-diol form of GA (K_{hyd} = [gem-diol form of GA]/[keto-form of GA] = 3.0×10^2 at 298 K),[54] with chloride. The area under each MS peak indicates that the abundance ratio of the anions B_{127} = 0.74 and B_{129} = 0.26 is related by the natural abundance of ^{35}Cl to ^{37}Cl.[55] (Figure S3A, Supporting Information). A similar result from the photolysis of 252.1 mM GA with electrolytes in air (Control N, Table S2, Supporting Information) reflects also an isotopic signature for one chlorine in the cluster: B_{127}/B_{129} = 0.74/0.26 (Figure S3B, Supporting Information). The change in the ion count for these two related peaks for variable fragmentor voltage is plotted in Figure S4 (Supporting Information), and clearly differs from the behavior of species assigned as products that have a maximum ion count between 40 and 60 V. In addition, because neither of the peaks at *m/z* 127 and 129 is detected in the IC-ESI-MS chromatograms, they are assumed to belong to the formation of ESI clusters. Therefore, the major new products from the cross reaction of PA and GA are the species with the molecular mass of 148, 162, and 164 Da. The formation of these three species requires the presence of both PA and GA to form C_5- and C_6-carboxylic acids with general formulas $C_5H_8O_5$, $C_6H_{10}O_5$, and $C_5H_8O_6$, respectively.

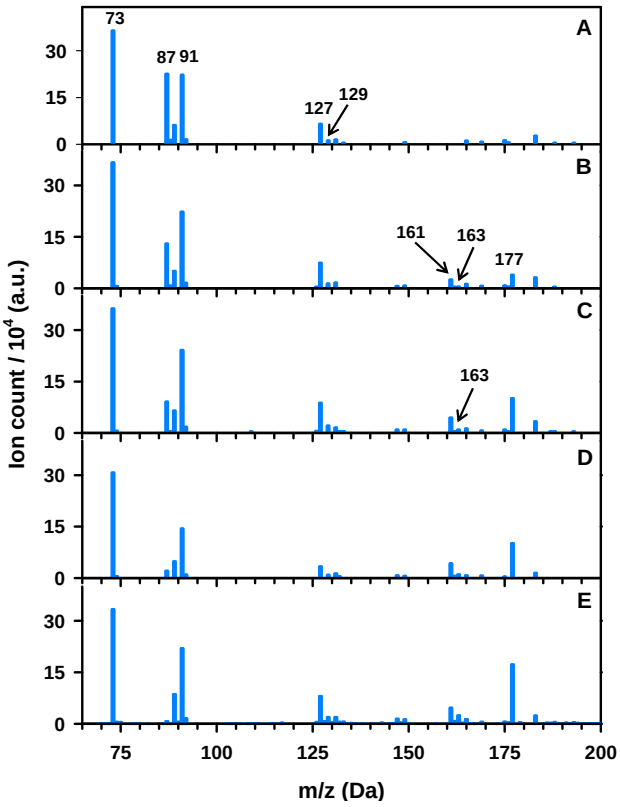

Figure 6. ESI-MS(-) spectra of the experiment in Figure 1 during stage I (Scheme 2) (A) before photolysis, and after (B) 1, (C) 2, (D) 4, and (E) 6 h of irradiation.

The use of NMR spectroscopy, including 1D ^{1}H- and ^{13}C-NMR, and 2D gCOSY and HSQC, provides additional structural information of the photolysis mixture. Experimental details are available in the Supporting Information. 2D NMR provides the chemical shift information from ^{1}H- and ^{13}C-NMR, and also offers the through-bond correlation between couples of protons on adjacent carbons in gCOSY measurements, and the correlation between proton and carbon via single-bond in HSQC experiments.[56] The same gCOSY method is applied to DSS internal standard (δ = 0.00 ppm), aqueous

PA, GA, and the mixture of PA and GA under the experimental conditions before and after photolysis.

The gCOSY spectra in Figure 7 are color coded for DSS (grey), PA (red), GA (green) and PA and GA mixture (blue) before (Figure 7A) and after irradiation (Figure 7B). From both combined spectra, no signal indicates the correlation of any two adjacent carbon atoms both having hydrogen atoms except the ones from DSS. The only coupled proton correlations are from the methylene groups in DSS (δ = 0.62, 1.77, and 2.92 ppm). Thus, it can conclude that there is no >CH-CH< groups in the product mixture. The signal intensity in Figure 7B at the cross point of 8.33 ppm, which corresponds to the range of aldehyde hydrogens, is considerably larger than in Figure 7A, pointing to the existence of photoproducts with aldehyde groups.

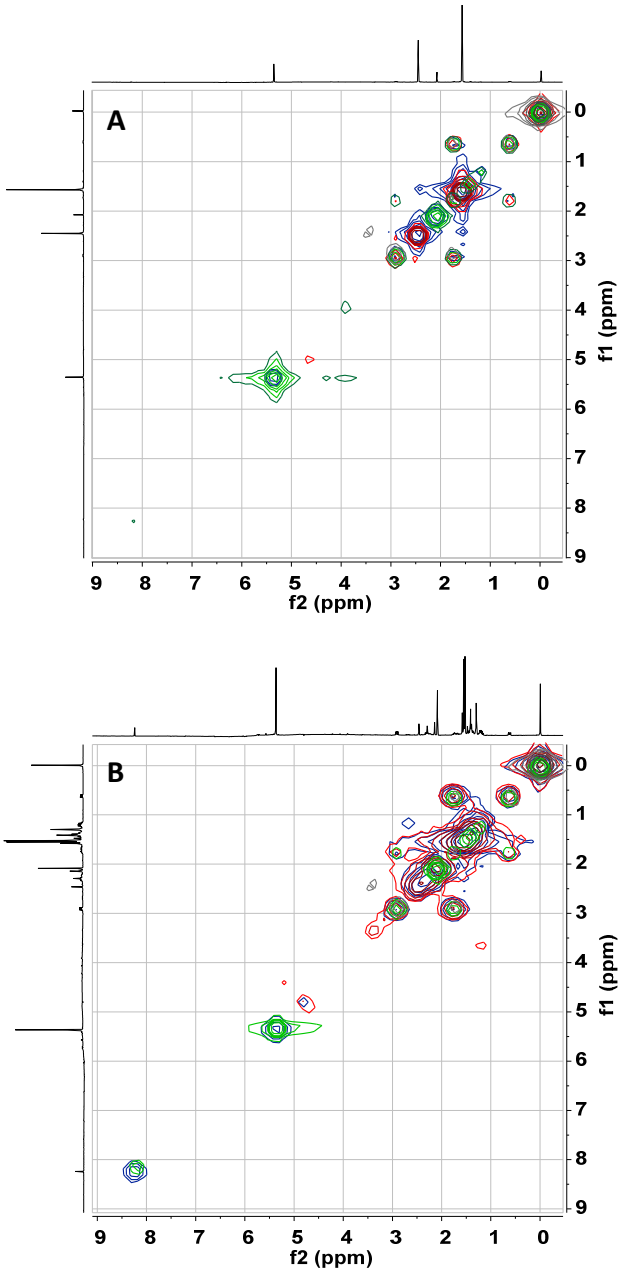

Figure 7. gCOSY spectra using WET suppression of 27.9 mM PA (red) and 235.6 mM GA (green) mixed solution (blue, experiment in Table 1) with DSS (grey) internal standard before (A) and after (B) 6 h photolysis. Both 1D and 2D spectra have solvent (water) peak subtracted.

Figure 8 displays the ^{13}C-NMR spectrum of a photolyzed mixture of PA and GA after 6 h irradiation (red trace) compared to the spectrum before photolysis (black trace). The signals at δ = 0.000, 17.594, 21.701, and 56.964 ppm corresponded to DSS. There are six peaks that belong to PA (the carbonyl form) and 2,2-dihydroxyproionic acid (2,2-DHPA, the gem-diol form of PA) at the following chemical shifts: 1) 28.496 and 27.891 ppm for the methyl groups, 2) 166.377 and 177.686 ppm for the carboxyl groups, 3) 95.412 ppm for the carbon with two hydroxyl groups in 2,2-DHPA, 4) 200.01 ppm for the carbonyl group in PA. For GA and its gem-diol, the carboxyl groups are found at δ = 194.090 and 179.400 ppm, respectively. The two large peaks at 88.894 and 175.886 ppm in the black trace of Figure 8 are related to the coexisting carbons on gem-diol and aldehyde groups of GA, respectively. After 6 h of irradiation, the peaks for PA and DHPA at 27.891, 28.496, 95.412, 177.686, 194.090 and 200.001 ppm disappear. Simultaneously, the intensity drop of GA and its gem-diol in equilibrium at δ = 88.894, 166.377, and 179.400 ppm indicate its loss. The red trace for products in Figure 8 reveals new signals in the region 155-185 ppm (165.891, 179.806, and 179.912 ppm) arising from carboxylic acids. The appearance of ether groups is evidenced by new peaks within the 40-80 ppm range[56] (δ = 70.278, 72.179, 77.397, 77.535, 79.489, 79.751) that grow during the post-irradiation period for the PA + GA mixture. Similar observations can be made for individual PA (control G, Figure S5, Supporting Information) and GA (control N, Figure S6, Supporting Information) experiments. Because GA is consumed over time during the cross photolysis reaction, as proved by the data in Figure 4, the large intensity peak for a carbonyl at δ = 175.895 ppm that practically overlaps the keto-form of GA reflects the formation of aldehyde products. This observation is also confirmed by the results in

Figure 7 that display the production of aldehydes. In summary, this data provides additional evidence that the C_5- and C_6-carboxylic acids of mass 148, 162, and 164 Da possess ether and aldehyde groups.

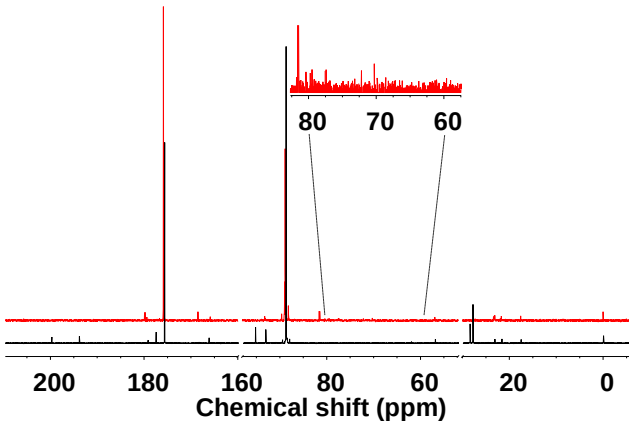

Figure 8. ^{13}C-NMR spectra for the experiment in Figure 1 (bottom black line) before and (top red line) after 6 h photolysis. The inset shows the spectrum in the range 55-85 ppm. No signals appear within the two excluded spectral brackets.

Figure 9 shows the change in total ion count over the different processing stages in Scheme 2 for the experiment with PA and GA. Initial photoproducts can be consumed during the second photolysis (Stage III), because of their chromophoric carbonyl groups. The lack of major changes in the mass composition observed in Figure 9 after Stage I indicates that persistent oligomers that resist further photoprocessing but that undergo reversible thermochromism and photobleaching are formed in water. However, the analysis of ^{13}C-NMR spectra over stages I-IV (Figure S1 in the Supporting Information) shows that some new peaks actually appear during stage III in the δ at 65-85 ppm range

corresponding to saturated carbon (sp^3), arising from hydrocarbons with ether groups,[56] and disappear during the following thermal aging (Stage IV). This versatility is provided by some complex products that may decompose and re-combine under sunlight irradiation, and that have some functional groups that can react in the dark with low activation energy.

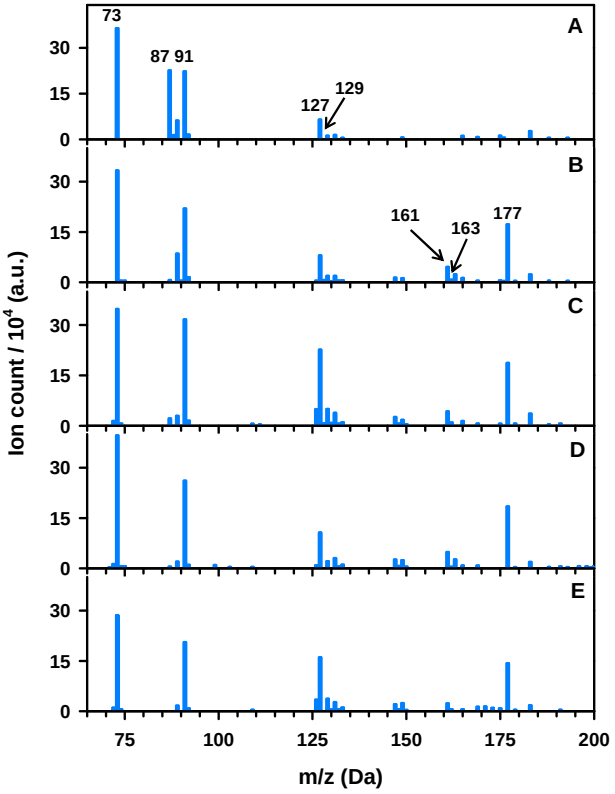

Figure 9. ESI-MS(-) spectra of the experiment in Figure 1 during stages I-IV (Scheme 2) (A) before photolysis, and (B) after 6 h irradiation in stage I, (C) at the end of the dark aging process in stage II, (D) after 6 h photolysis in stage III of panel C, and (E) after the completion of the aging process in stage IV.

Figure 10 explores whether the higher mass products are generated during different stages of processing. Data in red columns (Figure 10) shows how the total ion count integrated in the interval 50-850 Da varies over all stages. The total ion count, TIC, is calculated from

$$\mathrm{TIC} = \sum_{50}^{850} I_{\mathrm{i}} \tag{3}$$

where I_i is the ion count for individual peaks of mass i. The blue columns in Figure 10 show the change in average mass, $\overline{\mathrm{M}}$, calculated from

$$\overline{\mathrm{M}} = \frac{\sum_{50}^{850} m_i I_i}{\sum_{50}^{850} I_i} \tag{4}$$

where m_i stands for the mass of species i. It is clear that only for the transition from stage III to IV $\overline{\mathrm{M}}$ decreases while the total I_i increases, which matches earlier observations for the decomposition of PAphotoproducts during the aging process.[39] No heavier mass than 250 Da formed in the cross photoreaction of PA and GA. The change of $\overline{\mathrm{M}}$ is small after the first photolysis and may reflect that the loss of total organic carbon (TOC) during the whole process is due mainly to decarboxylation of PA with a quantum yield $\Phi = 0.78 \pm 0.01$ in water.[57]

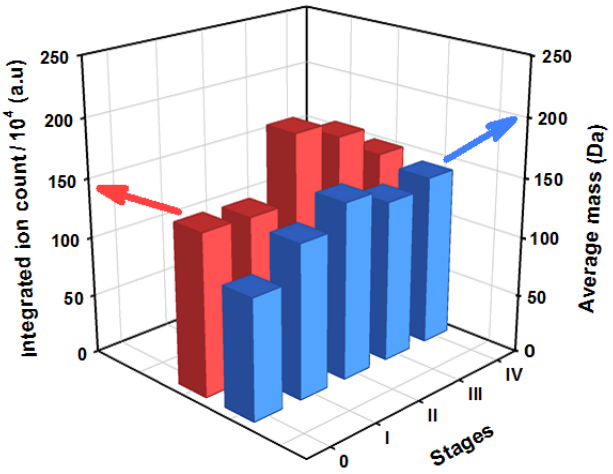

Figure 10. Total ion count (TIC) and average mass in the ESI-MS for the experiment in Figure 1 before photolysis and after the four stages in Scheme 2.

3.3 Mechanism of the cross photoreaction of PA and GA

From the learning disclosed in the discussion above and based on PA photolysis,[36,39] a mechanism for the cross reaction of PA and GA via radical chemistry is proposed in Scheme 3. First, PA is activated by light ($\lambda > 300$ nm) to produce singlet excited state $^1PA^*$, which undergoes intersystem crossing to a triplet $^3PA^*$ that has a lifetime of ~ 0.5 μs.[58] Then, $^3PA^*$ can react with the ground state of GA by photoinduced electron or hydrogen transfer to produce two possible triplet radical-ion pairs, $^3RP_1$ and $^3RP_2$.[36] After protonation and deprotonation steps for the radical anions and radical cations, respectively, two different ketyl ($K^\bullet$ and $Y^\bullet$) and oxyl ($X^\bullet$ and $Z^\bullet$) radicals can be formed. The major TOC loss of the entire process is related to the decarboxylation, which originates partially from the acyloxyl radicals $X^\bullet$ and $Z^\bullet$ that form acetyl radicals $Q^\bullet$ and $H^\bullet$, respectively. All these new radicals can combine with neutral molecules (PA, DHPA,

2-hydroxyacrylic acid, GA, etc.) to form secondary radicals, which combine with acetyl radicals ($Q^{\bullet}$ and $H^{\bullet}$) to form polyfunctional carboxylic acids. The resulting carboxylic acids can undergo rapid decarboxylation to produce C_5- and C_6- carboxylic acids, which also contribute to the loss of TOC. The formation of the products at *m/z* 147 and 161 originate from the pathways described above, based on the evidence of the detection for anions at *m/z* 191 and 205, which are the precursors of the respective products with *m/z* 147 and 161, respectively before decarboxylation. The product with the molecular mass of 164 Da is formed from the combination of two ketyl radicals, $K^{\bullet}$ and $Y^{\bullet}$. In addition, the self-reaction products of PA (2,3-dimethyltartaric acid) and GA (tartaric aicd) are included in the mechanism in Scheme 3.

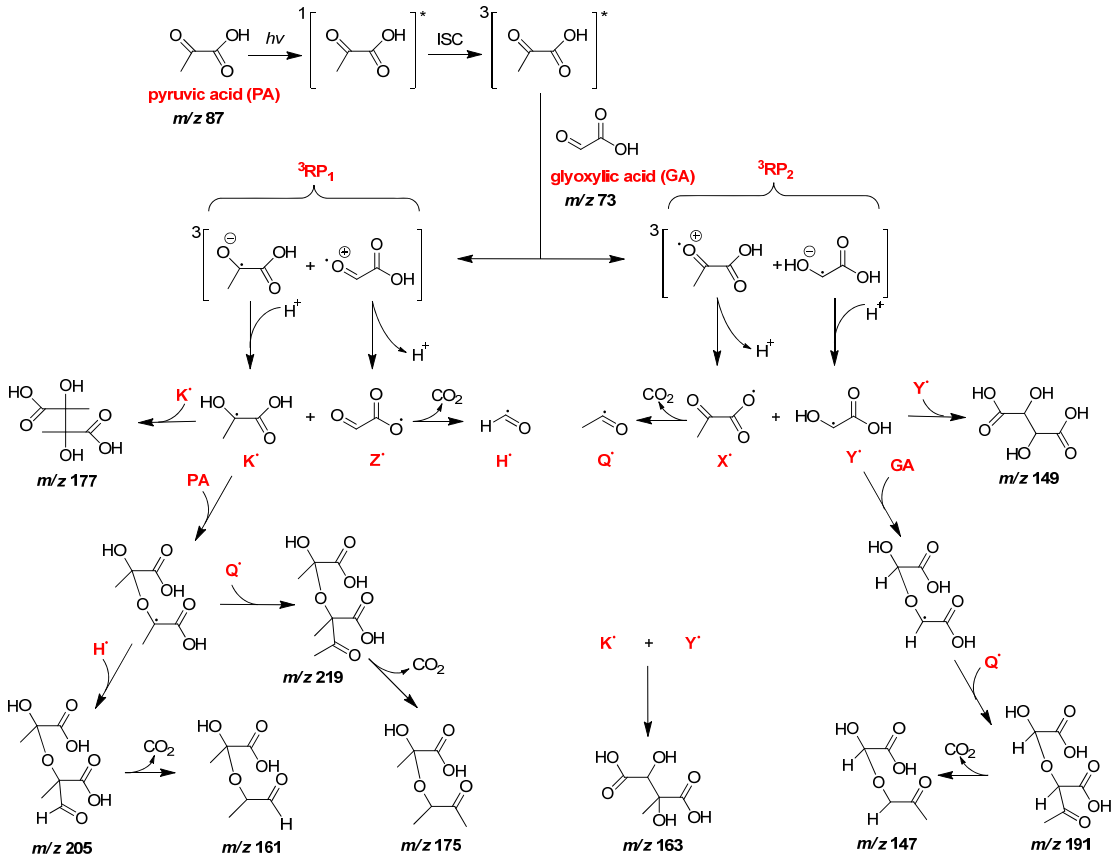

Scheme 3. Proposed mechanism for the cross reaction of aqueous PA and GA.

This work also considers an alternative mechanism involving H-abstraction from the gem-diol of PA by preformed radicals (Scheme S1), which is discarded based on the negative results for the detection of the hydrazones at *m/z* 253 and 267 in the UHPLC-ESI-MS chromatogram of derivatized photolysis samples with dinitrophenylhydrazine (DNPH) under the conditions reported by Eugene at al. (2013).[52] Finally, all the possibilities for the recombination of radicals and their addition to neutral molecules beyond Scheme 3 are presented in the Supporting Information (Schemes S2-S6), where isomeric products are considered.

Section 4: Conclusions

This thesis studies the cross photoreaction of PA and GA under simulated solar irradiation and the thermal processing of the photolyzed in the dark. The mechanism proposed via radicals of dicarbonyl species in water provides a plausible explanation for the generation of complex organic matter in aqueous aerosols by previously unknown pathways. This study reveals the cross reactivity of PA and GA to produce species with higher O/C ratios than observed for the self-reaction of PA or GA. PA can be considered to behave as a photosensitizer that induced the reactivity of GA, forming new species in model aqueous aerosols. Therefore, diverse reactive processes should be operative in tropospheric waters to produce aqSOA of higher structural complexity than the precursors. This information contributes new experimental evidence to explain the mechanisms of aqSOA production to constrain the gap between predictions and field measurements of SOAs.

Experiments and controls also explore the effects caused by inorganic electrolytes and [O_2(aq)]. The chemical identification and structural information is obtained from direct infusion ESI-MS, IC-ESI-MS, and NMR spectroscopy, and contrasted to studies of optical properties to propose a mechanism for the cross photoreaction in water. The mechanism involves the direct participation of radicals and explains the production of the major products, C_5- and C_6- carboxylic acids including carbonyl and ether functional groups. In addition to provide an explanation for all structures and formation pathways for the new products in the mechanism of Scheme 3, this work has considered other possibilities depicted in Schemes S1-S6.

The assignment of cross-reaction products is based on the comparison of experiments and controls for the self-reaction of each PA and GA. The production of species with molecular formula $C_5H_8O_5$ (148 Da), $C_6H_{10}O_5$ (162 Da), and $C_5H_8O_6$ (164 Da) is still very favorable in air (*vs.* in N_2) and enhanced in the presence of inorganic electrolytes. The cross reaction does not favor the production of the self-reaction product 2-(3-oxobutan-2-yloxy)-2-hydroxypropionate from PA but does not prevent it either, with the abundance ~ 34 times lower. However, the other self-reaction generated dimer of PA, 2,3-dimethyltartaric acid is still important during the cross reaction. The production of a trace of tartaric acid, a dimer of GA self-reaction, is detected. It is interesting to compare the range in the O/C ratio for the cross reaction (0.83-1.2) *vs.* the self-reaction of PA (0.71-1). This comparison shows that GA alters the reactivity channels when present together with PA in atmospheric aerosols, by increasing the formation of more oxygenated species. Because the only product detected in the self-reaction of GA irradiated aqueous solutions

is its dimer, tartaric acid, the higher promiscuity of GA in the presence of PA photosensitizer must cause the production of the three new products.

Reproducible photobleaching and thermochromism periods coincide with irradiation and thermal aging. The environmental implications of this study are related to the information describing the behavior of the optical properties of complex oligomers and the effect of inorganic electrolytes and dissolved O_2(aq) levels. It must be noticed that only an O_2(g) saturated atmosphere has a detrimental effect on the development of thermochromism. The absorbance of products increases as the [O_2(aq)] decreases following the order O_2(g) < air < N_2(g). However, for actual atmospheric conditions, thermochromism in N_2(g) is not significantly different than in air. A second important outcome of this work arises from the observation that successive dilutions after thermochromism demonstrates that Beer's Law is not followed in the visible spectrum. It is also concerning that for a P_{O_2} drop expected from an altitude increment, the violation of Beer's Law becomes more severe in the Earth's atmosphere, when comparing the results bracketed by the experiment in 1 atm air *vs.* control A in 1 atm N_2(g). In this regard, one must consider the optical properties of OAs to be affected by their variable and complex particle size, structure, and chemical composition. Accordingly, the direct and indirect effects of OAs on the Earth's energy balance are also variable.[10,16] Present findings from the cross reaction of PA and GA show that the optical properties vary independently, during daytime and nighttime cycles, from the chemical features of organic matter described by NMR spectroscopy in model aqueous aerosols. The observed behavior of model organic species should be treated in future climate change models taking into account thermochromism and photobleaching parametrization factors.

Section 5: Supporting Information

This section provides further details and explanations about the calculations and analyses performed. The material includes several supporting information tables, figures, and schemes accompanied by a brief discussion. The calculation for initial concentrations of PA and GA in the mixture via UV-visible absorption spectra is provided. The parameters for NMR analysis are defined. The tables, figures and schemes below include 1) controls for both PA and GA experiments, 2) ion chromatograms for both PA and GA photoreactions before and after irradiation, 3) the structures of the two diastereomers of 2,3-dimethyltartaric acid, 4) ^{1}H- and ^{13}C-NMR spectra for PA, GA, and a mixture of PA and GA mixture over the different stages in Scheme 2, 5) HSQC spectra for a mixture of PA and GA mixture after photolysis, 6) the ion count for variable fragmentor voltage in direct infusion ESI-MS, and 7) the alternative proposed mechanisms that considers H-abstraction from the gem-diol of PA.

List of Supporting Information Tables

List of Supporting Information Figures

List of Supporting Information Schemes

5.1. Calculation of initial concentrations of PA and GA in a mixture via UV-visible absorption spectroscopy

Actual initial concentrations of PA and GA in the mixture are determined by UV-visible absorption spectroscopy analysis using Beer's Law (Equation S1)

$$A = \varepsilon\, b\, [X] \tag{S1}$$

where ε is the molar absorptivity, b is the optical path length, and $[X]$ is the concentration of the component. Considering that the absorption bands of pure PA and pure GA significantly overlap in their mixture, a method to resolve their concentrations is introduced using a least square analysis. For this purpose, the individual spectra of standard [PA] = 28.8 mM and [GA] = 90.3 mM is recorded. The absorbance at wavelength λ = 260, 270, 280, 290, 300, and 320 nm from each one of the standards, and their mixture ($A_{m,}$ the same sample in Figure 1) is extracted. Then, the molar absorptivity of both PA and GA can be solved for each wavelength using Beer's Law. Spectral data is imported to a spreadsheet in Microsoft Excel for the previous purpose. Equation S2

$$A = \varepsilon(X)\, b\, [X] + \varepsilon(Y)\, b\, [Y] \tag{S2}$$

is employed to calculate the absorbance (A_{cal}) for the mixture of PA and GA at each wavelength from the estimated concentrations $[PA]_{guess}$ and $[GA]_{guess}$ (two estimated values). Then using the Microsoft Excel Solver function, the least square conditions, which minimize the sum of squares of $(A_{cal} - A_m)^2$ by iteratively varying the guess values $[PA]_{guess}$ and $[GA]_{guess}$, the solution to the concentrations in the mixture is

provided. The actual concentrations in the mixture are [PA] = 27.9 mM and [GA] = 235.6 mM. [56]

5.2. Experimental conditions for NMR analysis

For ^{1}H-NMR spectroscopy, data is collected at 298 K, with 32 K complex points, using a 90° pulse length (measured for each sample, ~ 14.5 μs). Thirty-two scans are acquired with a spectral width of 6.419 kHz, an acquisition time of 1.276 s, and a relaxation delay of 1.0 s. The WET method applied to all proton spectra is set up from the software VnmrJ 3.2 with a bandwidth of 100 MHz as indicated in Appendix I.

For ^{13}C-NMR spectroscopy, data is collected at 298 K, with 64 K complex points, using a 90° pulse length (measured for each sample, ~ 9.1 μs). About 24000 scans are acquired with a spectral width of 25.1731 kHz, an acquisition time of 1.302 s, and a relaxation delay of 1.0 s.

For 2D gCOSY and HSQC 2D-NMR experiments, the methods are built from the default experiments in VnmrJ 3.2 with the same conditions for proton and carbon spectra described above. The same WET method is also applied to proton spectra in 2D NMR.

5.3. Supporting tables and figures

Table S1. Controls with PA.

	Conditions				
			Atmosphere		
	$h\nu$ (2 h)	Electrolytes	Air	N_2	O_2
Control G	✓	✓	✓		
Control H	✓	✓		✓	
Control I	✓	✓			✓
Control J	✓		✓		
Control K	✓			✓	
Control L	✓				✓
Control M		✓	✓		

Key: $h\nu$ indicates the presence of light. Electrolytes include Na^+, Cl^- and SO_4^{2-}.

Table S2. Controls with GA.

	Conditions				
			Atmosphere		
	$h\nu$ (8 h)	Electrolytes	Air	N_2	O_2
Control N	✓	✓	✓		
Control O	✓	✓		✓	
Control P	✓	✓			✓
Control Q	✓		✓		
Control R	✓			✓	
Control S	✓				✓
Control T		✓	✓		

Key: $h\nu$ indicates the presence of light. Electrolytes include Na^+, Cl^- and SO_4^{2-}.

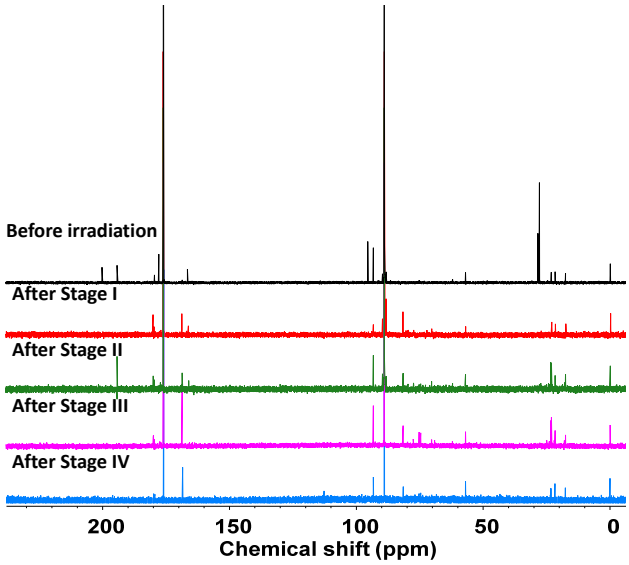

Figure S1. ^{13}C-NMR spectra of the experiment in Figure 1 during the four stages in Scheme 2.

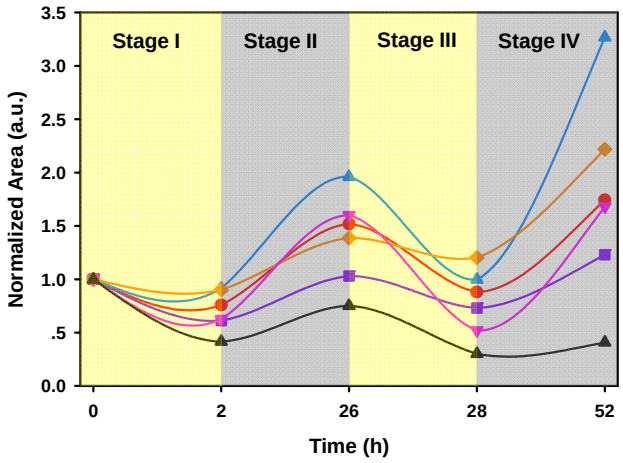

Figure S2. Normalized area of UV-visible absorption spectra from 295 nm to 500 nm for controls of PA photolysis in Table S1 for the four stages in Scheme 2. Key: (red ●) control G, (blue ▲) control H in N_2, (pink ▼) control I in O_2, (violet ■) control J without electrolytes, (orange ◆) control K without electrolytes in N_2, and (black ▲) control L without electrolytes in O_2.

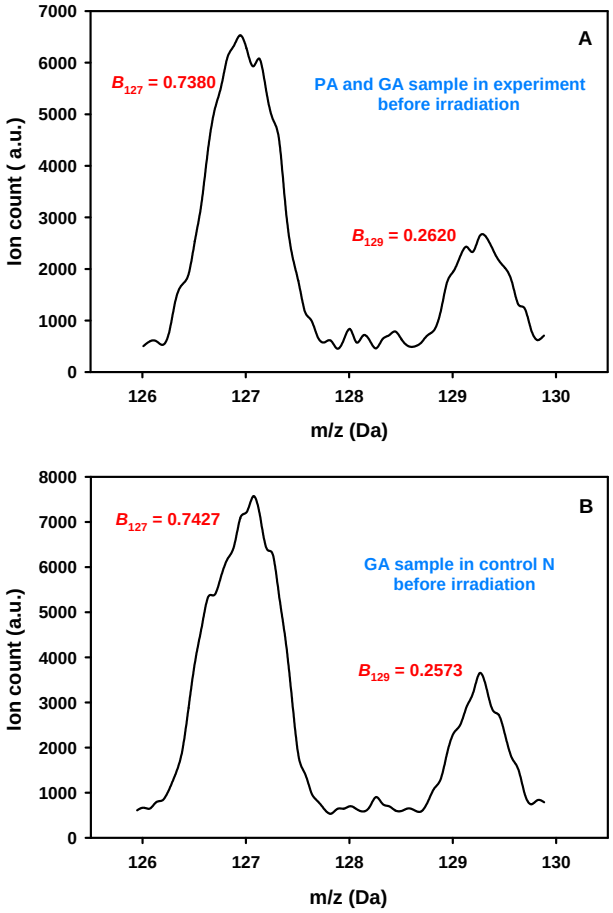

Figure S3. Areas under ESI-MS peaks with *m/z* 127 and 129 for samples before irradiation for (A) a mixture of PA and GA in the experiment and (B) GA solution in control N.

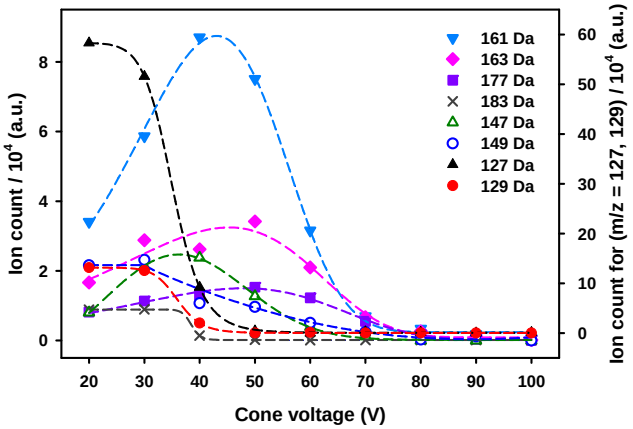

Figure S4. Ion count change for variable fragmentor voltage in direct infusion ESI-MS(-) for the experiment after stage I in Scheme 2.

In order to compare Figure 4 for the mixture of PA and GA with controls G and N, Figure S5 and S6 below present the products composition of direct photoinduced reactions for PA (Figure S5) and GA (Figure S6), respectively.

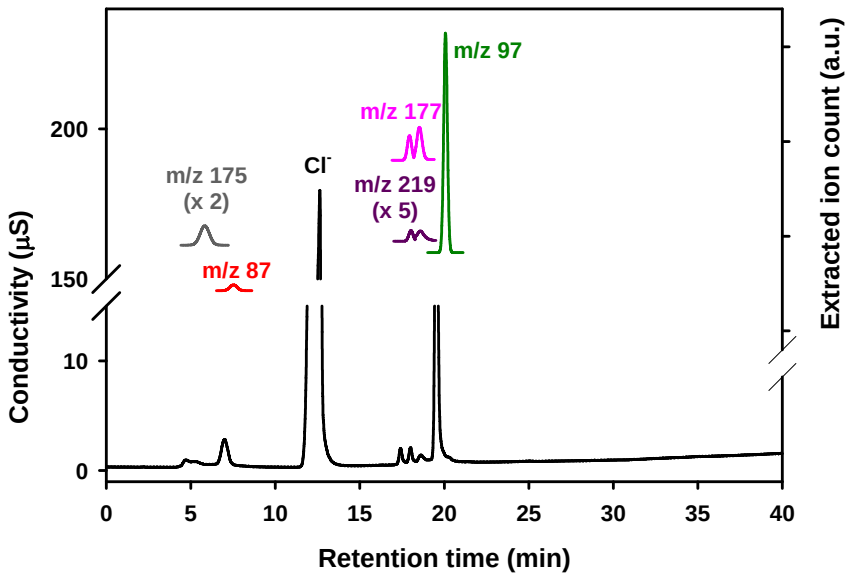

Figure S5. Ion chromatogram with conductivity and ESI-MS (-) detection for PA photoproducts with electrolytes in air (control G). The peaks in order of elution corresponded to the species 2-(3-oxobutan-2-yloxy)-2-hydroxypropionic acid, pyruvic acid, chloride, 2,3-dimethyltartaric acid and bisulfate.

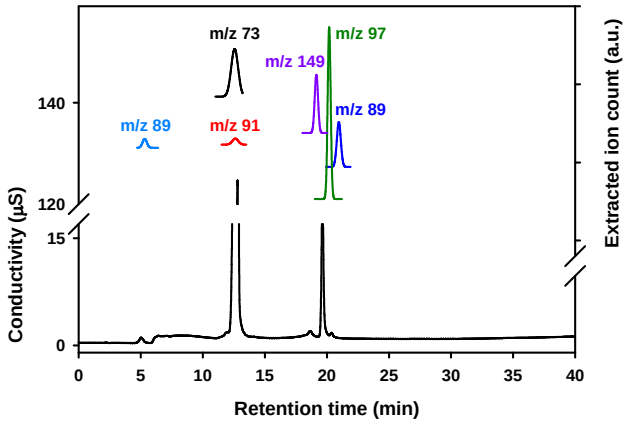

Figure S6. Ion chromatogram with conductivity and ESI-MS(-) detection for the photoproducts of GA with electrolytes in air (control N). The peaks in order of elution correspond to lactic acid, glyoxylic acid and its gem-diol form, tartaric acid, bisulfate and oxalic acid.

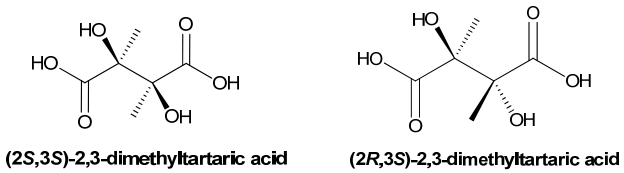

Figure S7. Structures of the two diastereomers of 2,3-dimethyltartaric acid (*m/z* 177).

The ^{13}C-NMR spectra for 1) PA (control G as in Figure S5) and 2) GA (control N as in Figure S6), both after photolysis are presented in Figures S8 and S9, respectively. The appearance of more -CH_3 signals in Figure S8 than in Figure 8, points to the fact that some minor products cannot form if GA is present during the photolysis of PA. Therefore, different mechanisms govern the major pathways for the cross reaction of PA and GA. Figure S10 shows the full ^{13}C-NMR spectra presented in the main text for the mixture of PA and GA in Figure 8.

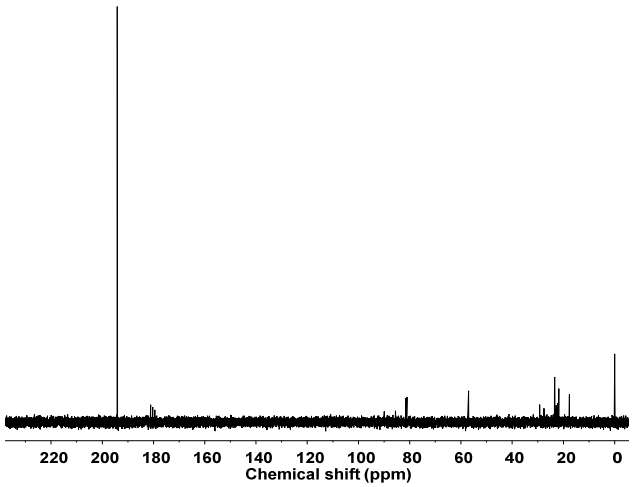

Figure S8. ^{13}C-NMR spectrum of PA post-irradiated sample of PA (control G) as in Figure S5.

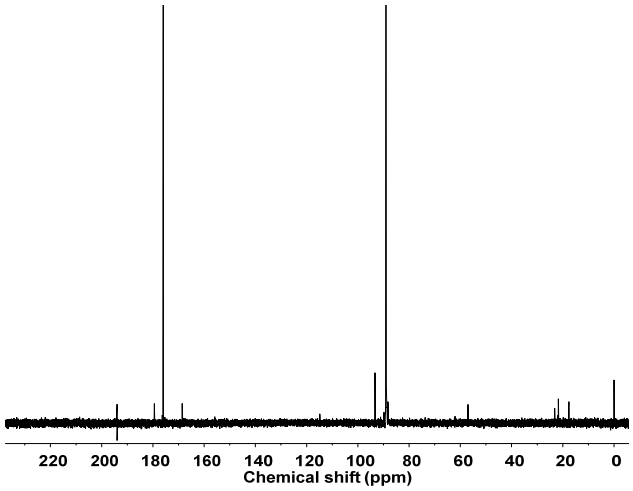

Figure S9. ^{13}C-NMR spectrum post-irradiated sample of GA (control N) as in Figure S6.

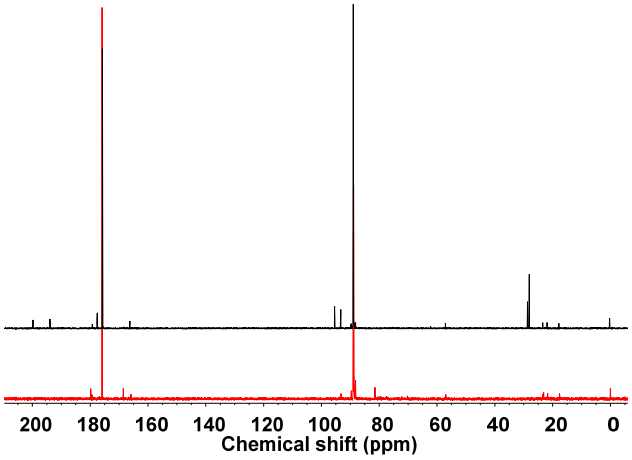

Figure S10. Full ^{13}C-NMR spectra for the experiment with a mixture of PA and GA displayed in Figure 8 before (top black trace) and after (bottom red trace) irradiation.

In Figure S11, S12A and S12B, ^{1}H-NMR spectra for the same experiment with a mixture of PA and GA displayed in Figure 8 is shown, as well as for the same PA post-irradiated sample in Figure S5 (control G) and the same GA photolyzed sample in Figure S6 (control N), respectively. ^{1}H-NMR spectra provide information of the hydrogen atoms located in different positions. In Figure S11, the peaks at δ = 8.25, 5.38, 2.46 and 1.58 ppm, correspond to GA, the gem-diol form of GA, the methyl groups of PA, and the methyl groups of the hydrated gem-diol form of PA, respectively. DSS at δ = 0.00 ppm is used as a reference. Figure S13 displays the HSQC spectrum of the experiment with a mixture of PA and GA as in Figure 8, which provides the correlation of protons and carbons via single-bond correlation.[56]

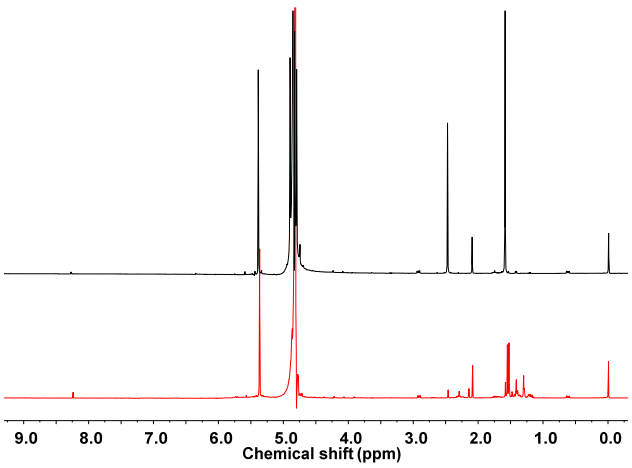

Figure S11. ^{1}H-NMR spectra for the experiment with a mixture of PA and GA (as in Figure 8) before (top black trace) and after 6 h photolysis (bottom red trace).

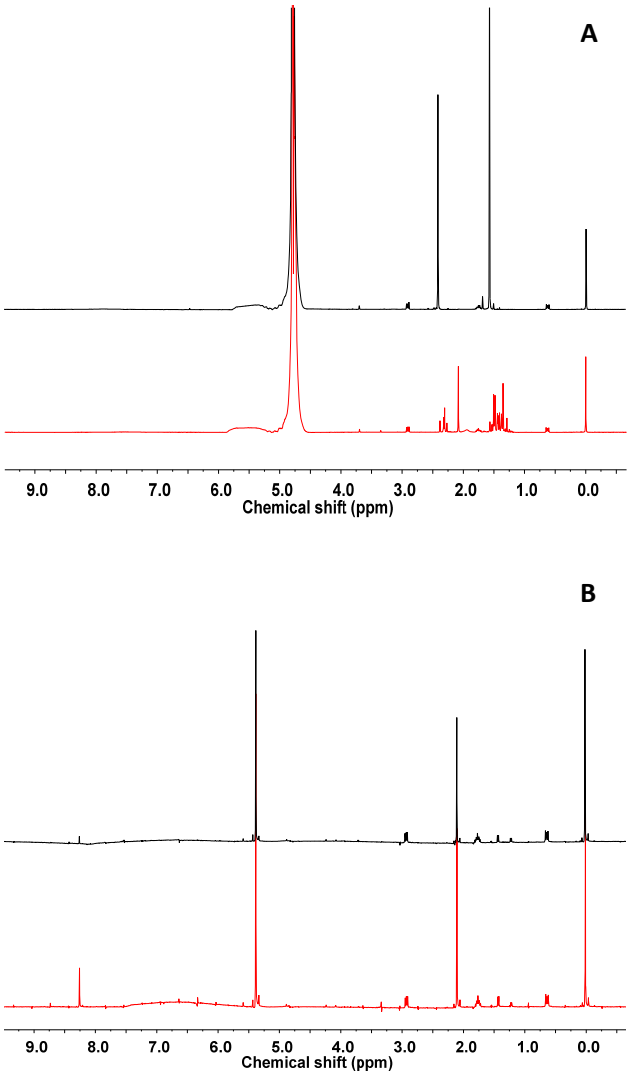

Figure S12. ^{1}H-NMR spectra of (A) same PA photoproducts in Figure S5 (control G) and (B) same GA post-irradiated sample in Figure S6 (control N). Solvent peaks are subtracted for better visualization of the gem-diol peak of GA.

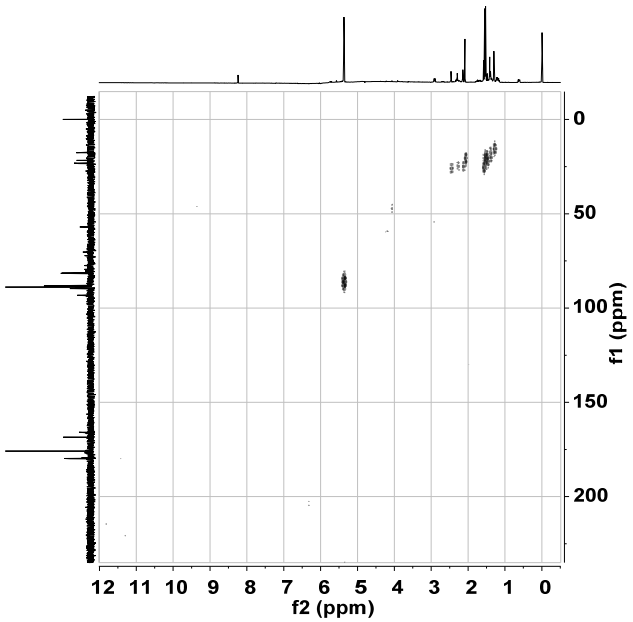

Figure S13. HSQC solvent (water) peak subtracted spectra of a mixture of 27.9 mM PA and 235.6 mM GA with electrolytes in air (experiment in Table 1) after 6 h photolysis (Stage I in Scheme 2).

Scheme S1 considers the possible H-abstraction from the gem-diol of PA from preformed radicals, in the mechanism of cross reaction of PA and GA. If this pathway would be of importance, the mechanism in Scheme S1 would predict the formation of intermediates and products with formula mass 136, 118, 150, 132, 88, and 74 Da. However, the final products acetoin (88 Da) and 2-hydroxypropanaldehyde (74 Da) possess a carbonyl that should have reacted with DNPH, and detected after chromatographic separation by UHPLC-ESI-MS.[52] In addition, the underivatized sample did not display the anions at *m/z* = 135, 117 and 131 in the IC-MS chromatogram. Therefore, it can be concluded that the mechanism in Scheme S1 is not competing with the proposed mechanism in Scheme 3.

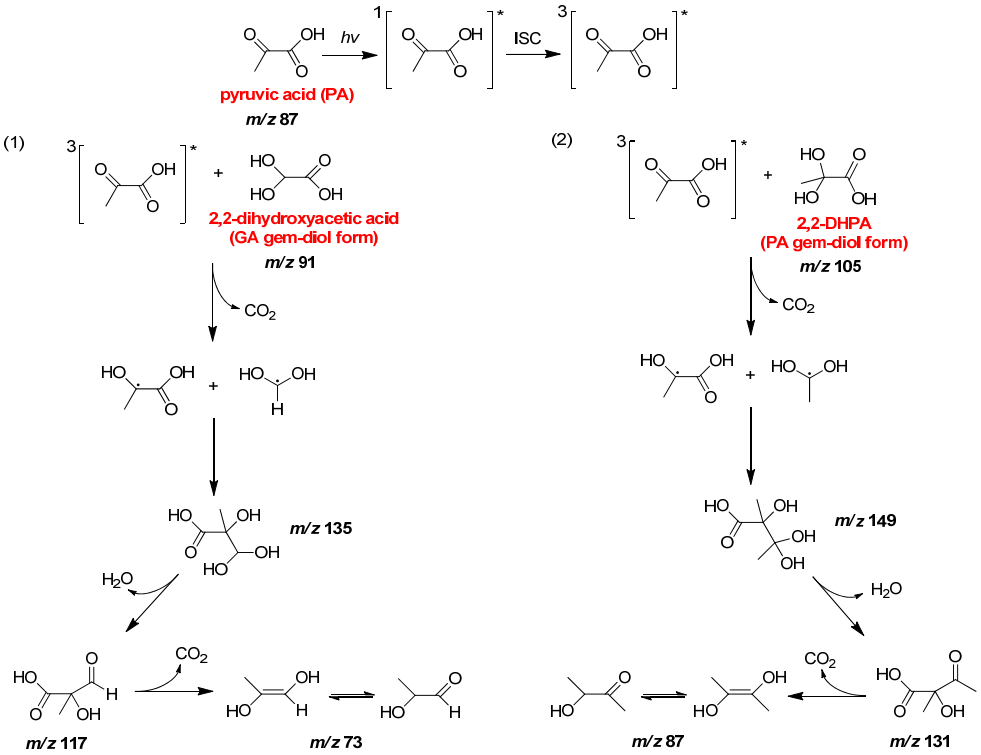

Scheme S1. Proposed mechanism for the cross reaction of aqueous PA and GA (experiment in Table 1) under the assumption of H-abstraction from the gem-diol of PA.

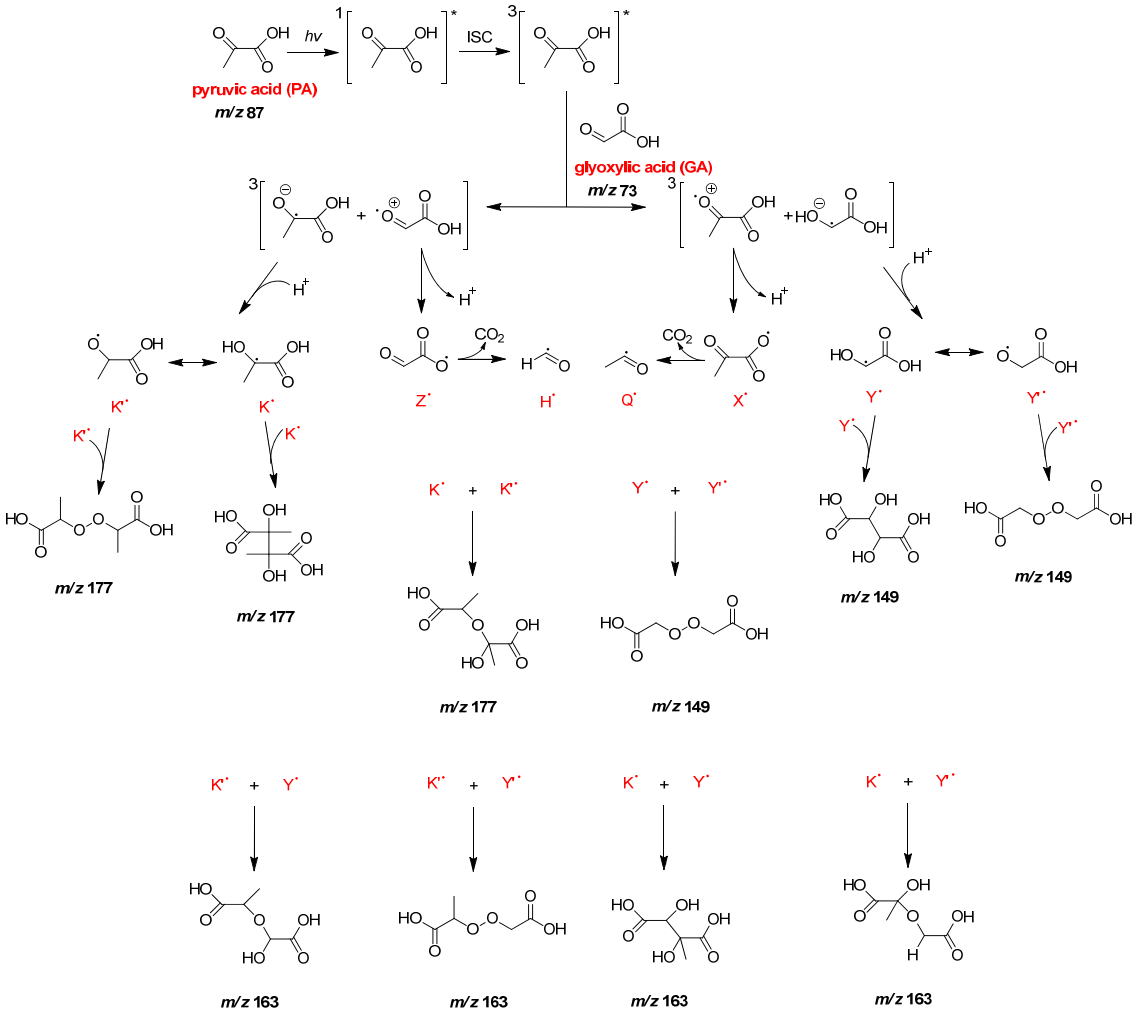

Scheme S2. Proposed mechanism for the cross reaction of aqueous PA and GA (experiment in Table 1) considering alternative pathways to those presented in Scheme 3.

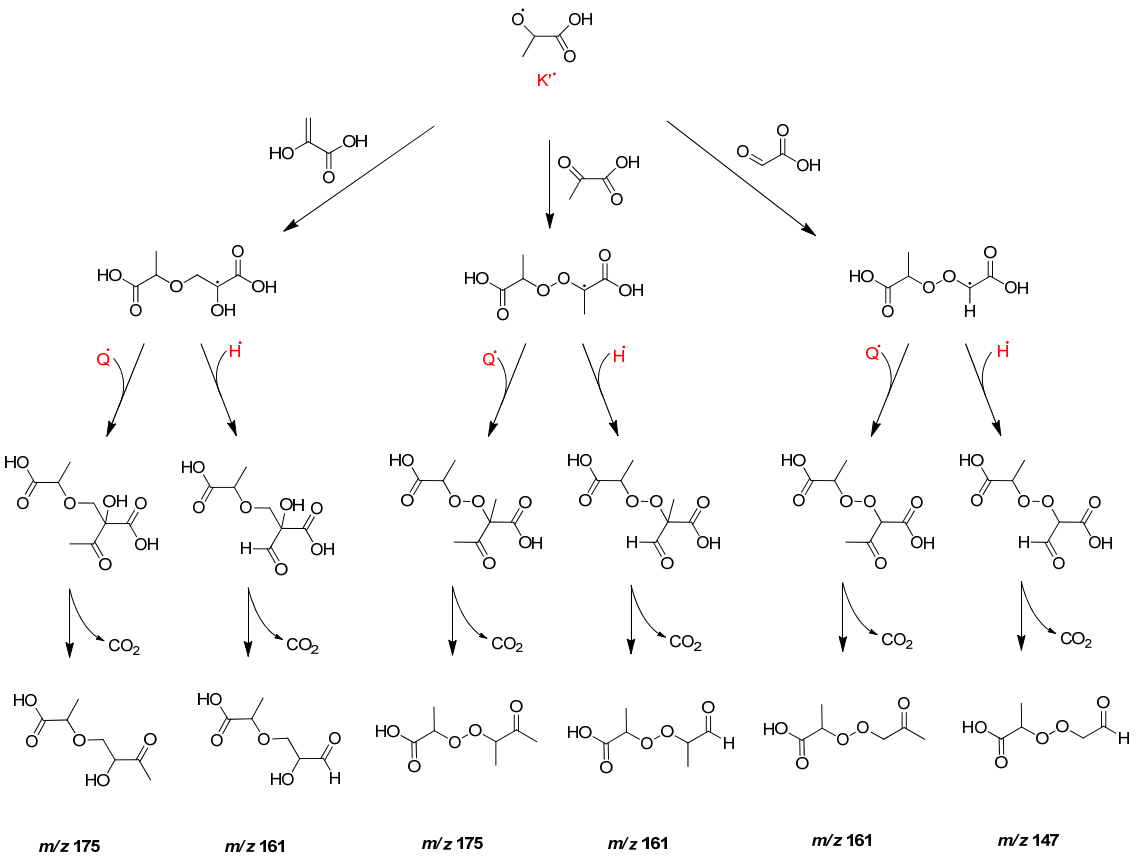

Scheme S3. Possible reactions of oxyl radical K'• from PA in Scheme S2 with neutral molecules.

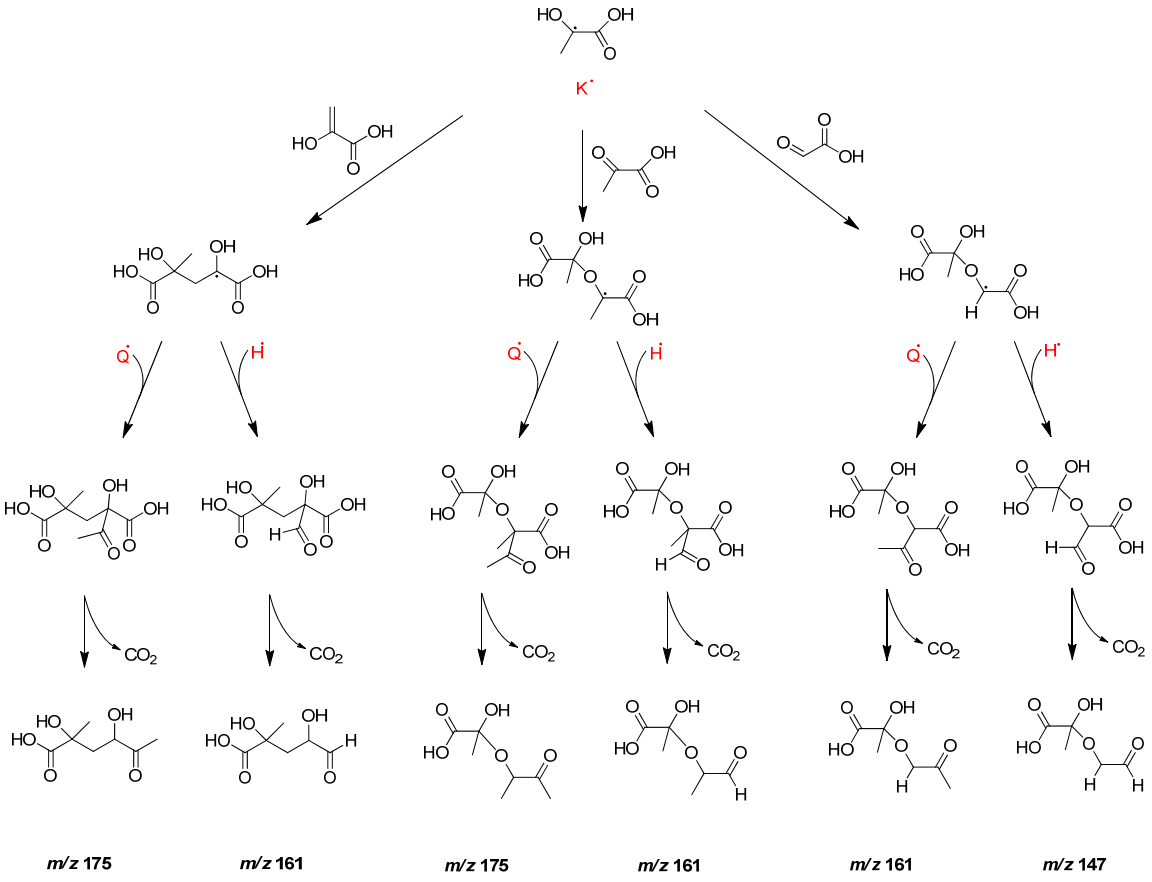

Scheme S4. Possible reactions of ketyl radical K$^{\bullet}$ from PA in Scheme S2 with neutral molecules.

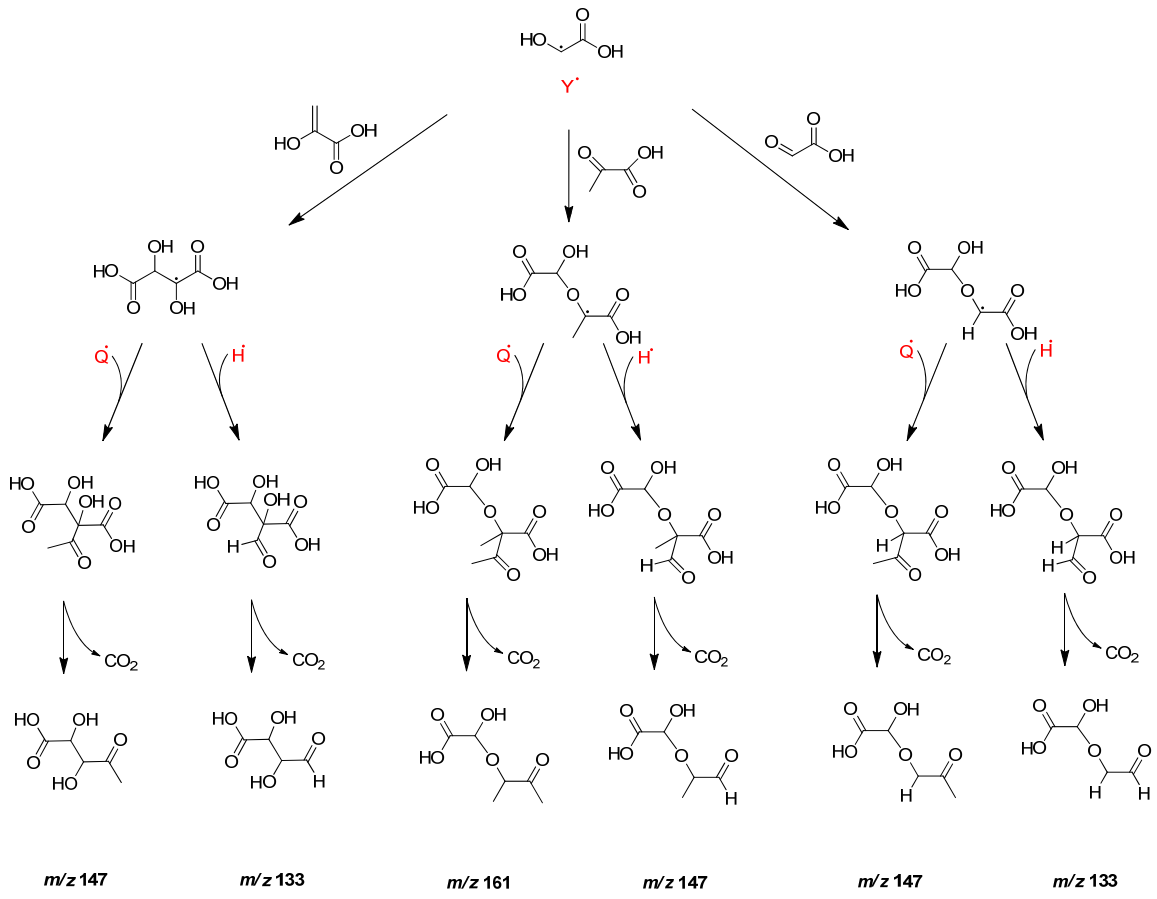

Scheme S5. Possible reactions of ketyl radical Y$^{\bullet}$ from GA in Scheme S2 with neutral molecules.

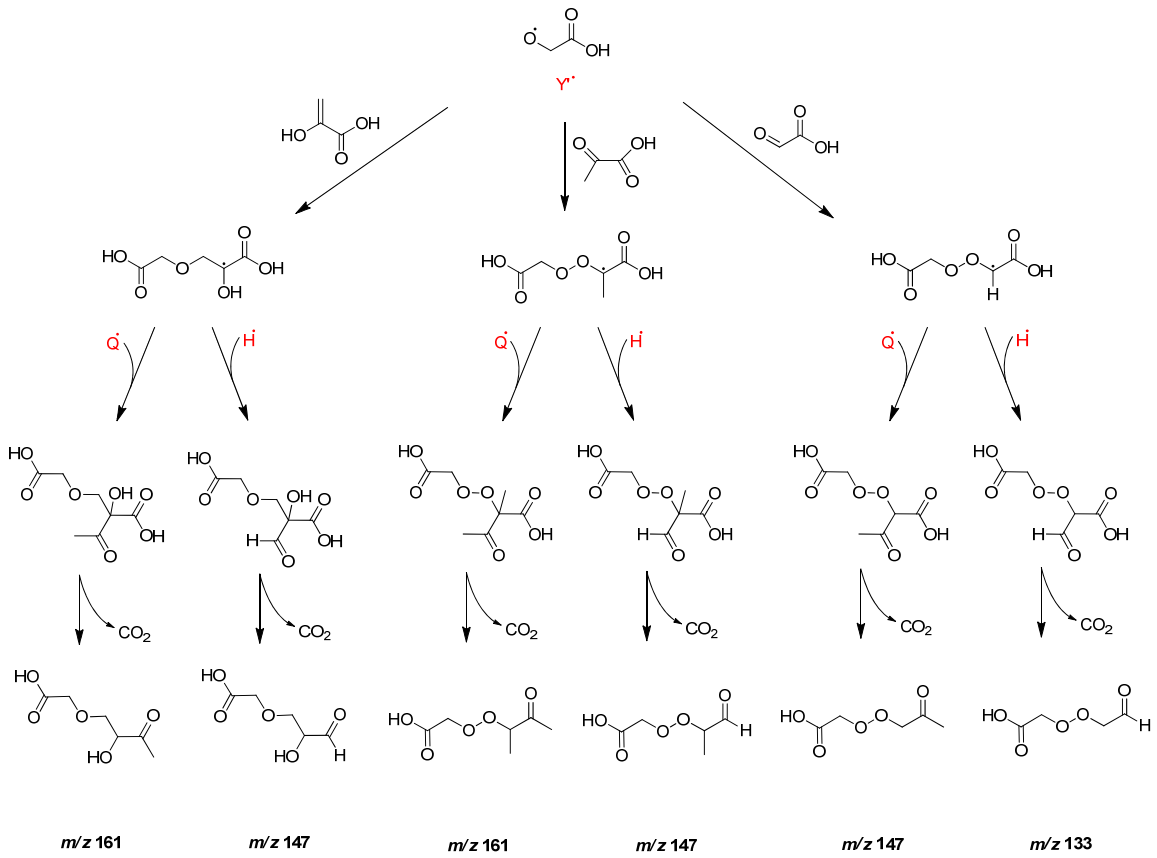

Scheme S6. Possible reactions of oxyl radical Y'• from GA in Scheme S2 with neutral molecules.

Appendix I

Reproduced from "A.J. Eugene, S.-S. Xia, and M.I. Guzman; **Negative production of acetoin in the photochemistry of aqueous pyruvic acid**, *Proceedings of the National Academy of Sciences* **2013**, *110*, E4274-E4275".

LETTER

Negative production of acetoin in the photochemistry of aqueous pyruvic acid

Recently, Griffith et al. reported that acetoin is a major product of the photolysis of aqueous pyruvic acid (PA), and proposed that its mechanism of formation involves the thermal decarboxylation of α-acetolactic acid (AL) intermediate (1). This finding is in contrast with a previous study by Guzman et al., based on experiments performed under similar conditions, which reported the formation of two major products: 2,3-dimethyl tartaric acid (**A**) and 2-(3-oxobutan-2-yloxy)-2-hydroxypropanoic acid (**B**) (2–4). Both **A** and **B** result after triplet radical pairs are formed via long-range (proton-coupled) electron transfer between carbonyl groups (5). Product **B** can thermally decompose into acetoin, but its carbonyl chromophore absorbs at $\lambda_{max} \sim 285$ nm vs. 276 nm for acetoin (2). In fact, Guzman et al. had shown that the thermal decarboxylation of aqueous AL proceeds at significantly slower rates than postphotolysis $CO_2(g)$ emissions, thereby excluding its participation in the mechanism of PA photolysis (2, 3).

A realistic reaction mechanism based on multiple spectroscopic features, such as those detected by Griffith et al. (1), should be able to identify intermediates and explain the reaction kinetics. Assigning spectroscopic features to specific carbonyls in complex mixtures is challenging at best and problematic in general. The standard procedure for the unequivocal identification of carbonyls, such as acetoin, involves the chromatographic separation of their 2,4-dinitrophenylhydrazone derivatives. Fig. 1 shows the chromatogram of a mixture produced from 1-h photolysis of 50 mM PA at 4 °C, followed by warming at 25 °C for 1 h, and subsequent derivatization with 2,4-dinitrophenylhydrazine. The *Z* and *E* hydrazones of PA elute at 4.60 and 6.40 min, and are seen in samples spiked with acetoin or unspiked. Acetoin is only observed at 5.80 min, when it is spiked before derivatization [$(\text{acetoin})_{final} = 20$ μM]. The absence of acetoin in the unspiked sample warrants that its yield, if produced, must be below 0.006%.

Inspection of the inset of figure 1 in Griffith et al. (1) makes it immediately apparent that the bands assigned to the trace species (overshadowed by water absorptions) do not match the spectrum of acetoin at multiple wavenumbers. Following a similar protocol to Griffith et al. (1), we obtained in Fig. 2 a better defined spectrum for the unknown species that partitions into the gas-phase (gray line), acetoin (blue line), and for a spike addition of acetoin to the product (red line). The spectrum of acetoin with a peak at 1,125 cm^{-1} does not match the spectrum of the photolysis product with a peak at 1,091 cm^{-1}, as is appreciated in the sample spiked with acetoin that causes the shoulder at 1,125 cm^{-1}. Therefore, we interpret Griffith et al.'s results (1) as in fact confirming that most of PA is converted to products **A** ($m/z = 177$) and **B** ($m/z = 175$) (2, 3), as displayed in figure S3 of ref. 1 which, in addition, lacks signals attributable to detectable amounts of lactate ($m/z = 89$) in the photolyzed sample.

ACKNOWLEDGMENTS. A.J.E. was supported in part by a Kentucky Opportunity Fellowship.

Alexis J. Eugene, Sha-Sha Xia, and Marcelo I. Guzman[1]

Department of Chemistry, University of Kentucky, Lexington, KY 40506-0055

1 Griffith EC, Carpenter BK, Shoemaker RK, Vaida V (2013) Photochemistry of aqueous pyruvic acid. *Proc Natl Acad Sci USA* 110(29):11714–11719.
2 Guzmán MI, Colussi AJ, Hoffmann MR (2006) Photoinduced oligomerization of aqueous pyruvic acid. *J Phys Chem A* 110(10): 3619–3626.
3 Guzmán MI, Hoffmann MR, Colussi AJ (2007) Photolysis of pyruvic acid in ice: Possible relevance to CO and CO_2 ice core record anomalies. *J Geophys Res Atmos* 112(D10):D10123.
4 Guzmán MI, Hildebrandt L, Colussi AJ, Hoffmann MR (2006) Cooperative hydration of pyruvic acid in ice. *J Am Chem Soc* 128(32): 10621–10624.
5 Guzmán MI, Colussi AJ, Hoffmann MR (2006) Photogeneration of distant radical pairs in aqueous pyruvic acid glasses. *J Phys Chem A* 110(3):931–935.

Author contributions: M.I.G. designed research; A.J.E., S.-S.X., and M.I.G. performed research; M.I.G. contributed new reagents/analytic tools; A.J.E. and M.I.G. analyzed data; and A.J.E. and M.I.G. wrote the paper.

The authors declare no conflict of interest.

[1]To whom correspondence should be addressed. E-mail: marcelo.guzman@uky.edu.

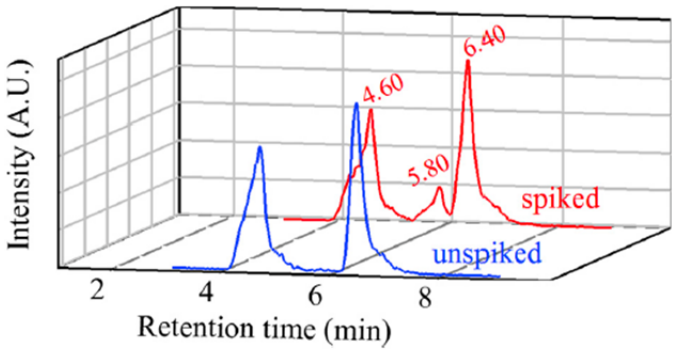

Fig. 1. Extracted ion (m/z = 267) chromatogram obtained by ultrahigh-performance liquid chromatography/electrospray ionization(-)/MS (Hypersil GOLD column 1.9 μm, 50 × 2.1 mm) of unspiked photolyzed sample (blue line) and 20 μM spiked acetoin for the same sample (red line) before derivatization. Retention times for the two hydrazones of PA and acetoin are 4.60, 6.40, and 5.80 min, respectively.

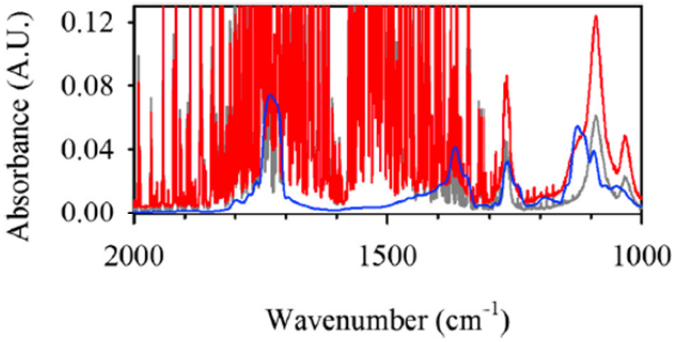

Fig. 2. Infrared spectrum of (gray line) collected gas over 50 mM aqueous PA after photolysis (λ > 305 nm) for 1 h, (blue line) acetoin and (red line) gas product spiked with acetoin.

Appendix II

A general method to build the WET solvent suppression method in VnmrJ 3.2 software is provided below.

WET--- water suppression enhanced through T1 effects

In VnmrJ 3.2, the operator should:

1. Open a regular proton experiment and measure accurate pw90 (90º pulse-width) value for the sample, and also write down the tpwr (transmitter power) number corresponding to that pw90. Here, no wet methods are activated and the gain value should be set to 0 to protect the probe.
2. After a full proton spectrum is collected, set the tof (transmitter offset) value at the chemical shift of water peak (position the cursor at the water peak and type “movetof” in the command box).
3. Go to “Experiment”, choose WET under solvent suppression.
4. Go to “Edit” then choose “New Pulse Sequence (PBox)”.
5. Click “New Waveform”.
6. Choose the method applied for solvent subtraction (usually “eburp1” will be used).
7. Enter the pw90 and tpwr values obtained from step 1 to the right top space called “Reference pw90” and “Reference tpwr”.
8. Set the bandwidth value and keep the remaining parameters unchanged.
9. Click “Add Waveform”. Check “z” and leave “x,y” unchecked. Click “Simulate it”.
10. Type the name for the shape file just built and click “Make it”.
11. Choose the “Acquisition” tab and go to “WET”.

12. Click “Update Waveform” in the PBox window.

13. Copy and paste the file name from the PBox window to the WET tab.

14. Under “Update Waveform”, click “Read Parameters” and enter the appearing parameters into the WET tab under “Acquisition”. (The power will be the coarse power.)

15. Now the power number in WET is an estimated one. It is better to run an array to measure the accurate value. The parameter for the array will be tpwr and set the starting value, increment and size for the array.

16. Before the array start, set gain = 10 (approximately) and have the WET method activated. Type “av” in the command box to show the absolute values of tpwr.

17. During the array, find the tpwr value which has the lowest peak for water. Enter the value to the WET tab for the WET power.

18. Type “ph” in the command box before running any regular spectra.

Note: The shape file built for WET method cannot be applied to all samples. It’s better to build individual shape files for different samples.

References

(1) Fiore, A. M.; Naik, V.; Spracklen, D. V.; Steiner, A.; Unger, N.; Prather, M.; Bergmann, D.; Cameron-Smith, P. J.; Cionni, I.; Collins, W. J. Global air quality and climate. *Chemical Society Reviews* **2012**, *41*, 6663-6683.

(2) Harrison, R. M.; Yin, J. Particulate matter in the atmosphere: which particle properties are important for its effects on health? *Science of the total environment* **2000**, *249*, 85-101.

(3) IPCC. Summary for Policymakers. In *Climate Change 2013: The Physical Science Basis. Contribution of Working Group I to the Fifth Assessment Report of the Intergovernmental Panel on Climate Change.*; 1st ed.; Cambridge University Press: New York, 2013; pp 3-29.

(4) Pope III, C. A.; Dockery, D. W. Health effects of fine particulate air pollution: lines that connect. *Journal of the Air & Waste Management Association* **2006**, *56*, 709-742.

(5) Atkinson, R. W.; Fuller, G. W.; Anderson, H. R.; Harrison, R. M.; Armstrong, B. Urban ambient particle metrics and health: a time-series analysis. *Epidemiology* **2010**, *21*, 501-511.

(6) Ramanathan, V.; Crutzen, P. New directions: Atmospheric brown "clouds". *Atmospheric Environment* **2003**, *37*, 4033-4035.

(7) Ramanathan, V.; Chung, C.; Kim, D.; Bettge, T.; Buja, L.; Kiehl, J.; Washington, W.; Fu, Q.; Sikka, D.; Wild, M. Atmospheric brown clouds: Impacts on South Asian climate and hydrological cycle. *Proceedings of the National Academy of Sciences of the United States of America* **2005**, *102*, 5326-5333.

(8) Lohmann, U.; Feichter, J. Global indirect aerosol effects: a review. *Atmospheric Chemistry and Physics* **2005**, *5*, 715-737.

(9) Boucher, O.; Randall, D.; Artaxo, P.; Bretherton, C.; Feingold, G.; Forster, P.; Kerminen, V.-M.; Kondo, Y.; Liao, H.; Lohmann, U. et al. Clouds and Aerosols. In *Climate Change 2013: The Physical Science Basis. Contribution of Working Group I to the Fifth Assessment Report of the Intergovernmental Panel on Climate Change.*; Cambridge University Press: New York, NY, 2013; pp 571-657.

(10) Kanakidou, M.; Seinfeld, J.; Pandis, S.; Barnes, I.; Dentener, F.; Facchini, M.; Dingenen, R. V.; Ervens, B.; Nenes, A.; Nielsen, C. Organic aerosol and global climate modelling: a review. *Atmospheric Chemistry and Physics* **2005**, *5*, 1053-1123.

(11) Kolb, C. E.; Worsnop, D. R. Chemistry and composition of atmospheric aerosol particles. *Annual review of physical chemistry* **2012**, *63*, 471-491.

(12) Ervens, B.; Turpin, B.; Weber, R. Secondary organic aerosol formation in cloud droplets and aqueous particles (aqSOA): a review of laboratory, field and model studies. *Atmospheric Chemistry and Physics* **2011**, *11*, 11069-11102.

(13) Shen, X.; Zhao, Y.; Chen, Z.; Huang, D. Heterogeneous reactions of volatile organic compounds in the atmosphere. *Atmospheric Environment* **2013**, *68*, 297-314.

(14) Hallquist, M.; Wenger, J.; Baltensperger, U.; Rudich, Y.; Simpson, D.; Claeys, M.; Dommen, J.; Donahue, N.; George, C.; Goldstein, A. The formation, properties and impact of secondary organic aerosol: current and emerging issues. *Atmospheric Chemistry and Physics* **2009**, *9*, 5155-5236.

(15) Scott, C. E.; Rap, A.; Spracklen, D. V.; Forster, P. M.; Carslaw, K. S.; Mann, G. W.; Pringle, K. J.; Kivekäs, N.; Kulmala, M.; Lihavainen, H. The direct and indirect radiative

effects of biogenic secondary organic aerosol. *Atmospheric Chemistry and Physics* **2014**, *14*, 447-470.

(16) Myhre, G.; Shindell, D.; Bréon, F.-M.; Collins, W.; Fuglestvedt, J.; Huang, J.; Koch, D.; Lamarque, J.-F.; Lee, D.; Mendoza, B. et al. Anthropogenic and Natural Radiative Forcing. In *Climate Change 2013: The Physical Science Basis. Contribution of Working Group I to the Fifth Assessment Report of the Intergovernmental Panel on Climate Change*; Cambridge University Press: New York, 2013; pp 659-740.

(17) Volkamer, R.; Jimenez, J. L.; San Martini, F.; Dzepina, K.; Zhang, Q.; Salcedo, D.; Molina, L. T.; Worsnop, D. R.; Molina, M. J. Secondary organic aerosol formation from anthropogenic air pollution: Rapid and higher than expected. *Geophysical Research Letters* **2006**, *33*, L17811.

(18) Goldstein, A. H.; Galbally, I. E. Known and unexplored organic constituents in the earth's atmosphere. *Environmental science & technology* **2007**, *41*, 1514-1521.

(19) Carlton, A. G.; Turpin, B. J.; Altieri, K. E.; Seitzinger, S. P.; Mathur, R.; Roselle, S. J.; Weber, R. J. CMAQ model performance enhanced when in-cloud secondary organic aerosol is included: Comparisons of organic carbon predictions with measurements. *Environmental science & technology* **2008**, *42*, 8798-8802.

(20) Wang, Q.; Jacob, D.; Fisher, J.; Mao, J.; Leibensperger, E.; Carouge, C.; Sager, P. L.; Kondo, Y.; Jimenez, J.; Cubison, M. Sources of carbonaceous aerosols and deposited black carbon in the Arctic in winter-spring: implications for radiative forcing. *Atmospheric Chemistry and Physics* **2011**, *11*, 12453-12473.

(21) Heald, C. L.; Coe, H.; Jimenez, J. L.; Weber, R. J.; Bahreini, R.; Middlebrook, A. M.; Russell, L. M.; Jolleys, M.; Fu, T.-M.; Allan, J. D. Exploring the vertical profile of

atmospheric organic aerosol: comparing 17 aircraft field campaigns with a global model. *Atmospheric Chemistry and Physics* **2011**, *11*, 12673-12696.

(22) De Gouw, J.; Jimenez, J. L. Organic aerosols in the Earth's atmosphere. *Environmental science & technology* **2009**, *43*, 7614-7618.

(23) Lim, Y.; Tan, Y.; Perri, M.; Seitzinger, S.; Turpin, B. Aqueous chemistry and its role in secondary organic aerosol (SOA) formation. *Atmospheric Chemistry and Physics* **2010**, *10*, 10521-10539.

(24) Carlton, A. G.; Turpin, B. J.; Lim, H. J.; Altieri, K. E.; Seitzinger, S. Link between isoprene and secondary organic aerosol (SOA): Pyruvic acid oxidation yields low volatility organic acids in clouds. *Geophysical Research Letters* **2006**, *33*, L06822.

(25) Ervens, B.; Carlton, A. G.; Turpin, B. J.; Altieri, K. E.; Kreidenweis, S. M.; Feingold, G. Secondary organic aerosol yields from cloud-processing of isoprene oxidation products. *Geophysical Research Letters* **2008**, *35*, L02816.

(26) Nguyen, T. B.; Bateman, A. P.; Bones, D. L.; Nizkorodov, S. A.; Laskin, J.; Laskin, A. High-resolution mass spectrometry analysis of secondary organic aerosol generated by ozonolysis of isoprene. *Atmospheric Environment* **2010**, *44*, 1032-1042.

(27) Martín-Reviejo, M.; Wirtz, K. Is benzene a precursor for secondary organic aerosol? *Environmental science & technology* **2005**, *39*, 1045-1054.

(28) Bloss, C.; Wagner, V.; Jenkin, M.; Volkamer, R.; Bloss, W.; Lee, J.; Heard, D.; Wirtz, K.; Martin-Reviejo, M.; Rea, G. Development of a detailed chemical mechanism (MCMv3. 1) for the atmospheric oxidation of aromatic hydrocarbons. *Atmospheric Chemistry and Physics* **2005**, *5*, 641-664.

(29) Warneck, P. Multi-phase chemistry of C2 and C3 organic compounds in the marine atmosphere. *Journal of atmospheric chemistry* **2005**, *51*, 119-159.

(30) Stefan, M. I.; Bolton, J. R. Reinvestigation of the acetone degradation mechanism in dilute aqueous solution by the UV/H_2O_2 process. *Environmental science & technology* **1999**, *33*, 870-873.

(31) Kawamura, K.; Tachibana, E.; Okuzawa, K.; Aggarwal, S.; Kanaya, Y.; Wang, Z. High abundances of water-soluble dicarboxylic acids, ketocarboxylic acids and α-dicarbonyls in the mountaintop aerosols over the North China Plain during wheat burning season. *Atmospheric Chemistry and Physics* **2013**, *13*, 8285-8302.

(32) Fu, P.; Kawamura, K.; Usukura, K.; Miura, K. Dicarboxylic acids, ketocarboxylic acids and glyoxal in the marine aerosols collected during a round-the-world cruise. *Marine Chemistry* **2013**, *148*, 22-32.

(33) Mkoma, S.; Kawamura, K. Molecular composition of dicarboxylic acids, ketocarboxylic acids, α-dicarbonyls and fatty acids in atmospheric aerosols from Tanzania, East Africa during wet and dry seasons. *Atmospheric Chemistry and Physics* **2013**, *13*, 2235-2251.

(34) Saxena, P.; Hildemann, L. M. Water absorption by organics: Survey of laboratory evidence and evaluation of UNIFAC for estimating water activity. *Environmental science & technology* **1997**, *31*, 3318-3324.

(35) Jang, M.; Czoschke, N. M.; Northcross, A. L. Atmospheric Organic Aerosol Production by Heterogeneous Acid-Catalyzed Reactions. *ChemPhysChem* **2004**, *5*, 1646-1661.

(36) Guzman, M.; Colussi, A.; Hoffmann, M. Photoinduced oligomerization of aqueous pyruvic acid. *Journal of Physical Chemistry A* **2006**, *110*, 3619-3626.

(37) Kawamura, K.; Imai, Y.; Barrie, L. A. Photochemical production and loss of organic acids in high Arctic aerosols during long-range transport and polar sunrise ozone depletion events. *Atmospheric Environment* **2005**, *39*, 599-614.

(38) Kawamura, K.; Yasui, O. Diurnal changes in the distribution of dicarboxylic acids, ketocarboxylic acids and dicarbonyls in the urban Tokyo atmosphere. *Atmospheric Environment* **2005**, *39*, 1945-1960.

(39) Rincón, A. G.; Guzmán, M. I.; Hoffmann, M. R.; Colussi, A. Optical absorptivity versus molecular composition of model organic aerosol matter. *Journal of Physical Chemistry A* **2009**, *113*, 10512-10520.

(40) Harvey, H. W. *The chemistry and fertility of sea waters*, 2nd ed.; Cambridge University Press: New York, NY, 1957.

(41) Hatchard, C.; Parker, C. A. A new sensitive chemical actinometer. II. Potassium ferrioxalate as a standard chemical actinometer. *Proceedings of the Royal Society of London. Series A. Mathematical and Physical Sciences* **1956**, *235*, 518-536.

(42) Harris, D. C. *Quantitative chemical analysis*, 7th ed.; W. H. Freeman: New York, NY, 2007.

(43) Li, K.; Stefan, M. I.; Crittenden, J. C. UV photolysis of trichloroethylene: Product study and kinetic modeling. *Environmental science & technology* **2004**, *38*, 6685-6693.

(44) Zhou, R.; Guzman, M. I. CO_2 Reduction under Periodic Illumination of ZnS. *Journal of Physical Chemistry C* **2014**, *34*, 11649-11656.

(45) Shapiro, E. L.; Szprengiel, J.; Sareen, N.; Jen, C. N.; Giordano, M. R.; McNeill, V. F. Light-absorbing secondary organic material formed by glyoxal in aqueous aerosol mimics. *Atmospheric Chemistry and Physics* **2009**, *9*, 2289-2300.

(46) Noziere, B.; Dziedzic, P.; Córdova, A. Products and kinetics of the liquid-phase reaction of glyoxal catalyzed by ammonium ions (NH_4^+). *Journal of Physical Chemistry A* **2008**, *113*, 231-237.

(47) Jones, M.; Fleming, S. A. *Organic Chemistry*, 4th ed.; W. W. Norton & Company Incorporated: New York, NY, 2010.

(48) Minerath, E. C.; Casale, M. T.; Elrod, M. J. Kinetics feasibility study of alcohol sulfate esterification reactions in tropospheric aerosols. *Environmental science & technology* **2008**, *42*, 4410-4415.

(49) Kropp, P. J.; Reardon, E. J.; Gaibel, Z. L.; Williard, K. F.; Hattaway, J. H. Photochemistry of alkenes. Direct irradiation in hydroxylic media. *Journal of the American Chemical Society* **1973**, *95*, 7058-7067.

(50) Rincón, A. G.; Guzmán, M. I.; Hoffmann, M.; Colussi, A. Thermochromism of model organic aerosol matter. *Journal of Physical Chemistry Letters* **2009**, *1*, 368-373.

(51) Manahan, S. E. *Environmental chemistry*, 9th ed.; CRC press: Boca Raton, FL, 2010.

(52) Eugene, A. J.; Xia, S.-S.; Guzman, M. I. Negative production of acetoin in the photochemistry of aqueous pyruvic acid. *Proceedings of the National Academy of Sciences* **2013**, *110*, E4274-E4275.

(53) Engel, T.; Reid, P.; McQuarrie, D. A. *Thermodynamics, statistical thermodynamics, and kinetics*, 2nd ed.; Prentice Hall, 2009.

(54) Sorensen, P. E.; Bruhn, K.; Lindelov, F. Kinetics and equilibria for the reversible hydration of the aldehyde group in glyoxylic acid. *Acta Chemica Scandinavica A* **1974**, *28*, 162-168.

(55) Shields, W. R.; Murphy, T. J.; Garner, E. L.; Dibeler, V. H. Absolute isotopic abundance ratio and the atomic weight of chlorine. *Journal of the American Chemical Society* **1962**, *84*, 1519-1522.

(56) Pavia, D.; Lampman, G.; Kriz, G. *Introduction to spectroscopy*, 3rd ed.; Brooks/Cole USA, 2003.

(57) Guzmán, M.; Hoffmann, M.; Colussi, A. Photolysis of pyruvic acid in ice: Possible relevance to CO and CO_2 ice core record anomalies. *Journal of Geophysical Research: Atmospheres (1984–2012)* **2007**, *112*, D10123.

(58) Guzman, M. I.; Colussi, A.; Hoffmann, M. R. Photogeneration of distant radical pairs in aqueous pyruvic acid glasses. *The Journal of Physical Chemistry A* **2006**, *110*, 931-935.

Curriculum Vitae

Shasha Xia

Education:

2011-2014: Master of Science, Department of Chemistry, University of Kentucky

2007-2011: Bachelor of Science, Department of Chemistry, Nankai University, China

Professional positions:

2011-2014: Teaching Assistant, Department of Chemistry, University of Kentucky

2012-2014: Research Assistant, Department of Chemistry, University of Kentucky

Professional publications:

Eugene, A. J.; Xia, S.-S.; Guzman, M. I. Negative production of acetoin in the photochemistry of aqueous pyruvic acid. *Proceedings of the National Academy of Sciences* **2013**, *110*, E4274-E4275.